JGR Atmospheres

RESEARCH ARTICLE
10.1029/2021JD035629

Key Points:

- The backscattering optical properties of dust aerosols were modeled systematically using homogeneous super-spheroids
- A comprehensive survey of the lidar ratio-depolarization ratio relations produced by super-spheroids at 355 nm wavelength was conducted
- Super-spheroids could be used to explain the wide variation of dust optical properties found in the high spectral resolution lidar data

Correspondence to:
K. Sato,
sato@riam.kyushu-u.ac.jp

Citation:
Kong, S., Sato, K., & Bi, L. (2022). Lidar ratio–depolarization ratio relations of atmospheric dust aerosols: The super-spheroid model and high spectral resolution lidar observations. *Journal of Geophysical Research: Atmospheres*, *127*, e2021JD035629. https://doi.org/10.1029/2021JD035629

Received 29 JUL 2021
Accepted 24 JAN 2022

Lidar Ratio–Depolarization Ratio Relations of Atmospheric Dust Aerosols: The Super-Spheroid Model and High Spectral Resolution Lidar Observations

Senyi Kong[1], Kaori Sato[2], and Lei Bi[1]

[1]Key Laboratory of Geoscience Big Data and Deep Resource of Zhejiang Province, School of Earth Sciences, Zhejiang University, Hangzhou, China, [2]Research Institute for Applied Mechanics, Kyushu University, Fukuoka, Japan

Abstract The backscattering optical properties of an ensemble of randomly oriented dust particles at a wavelength of 355 nm were comprehensively studied by examining the invariant imbedding T-matrix results of the super-spheroid dust model. In particular, we focused on the lidar ratio (S) and depolarization ratio (δ) relations of dust aerosols to aid interpretation of data from the Atmospheric Lidar (ATLID) instrument that will be onboard the Earth Cloud, Aerosol and Radiation Explorer (EarthCARE) satellite. Super-spheroid models with various aspect ratios (α), roundness parameters (n), and refractive indices were investigated over a wide range of particle sizes and compared to the observation data of the National Aeronautics and Space Administration (NASA) Langley 355-nm airborne high spectral resolution lidar. We found that super-spheroid dust particles with different sets of n and α could be used to model almost the entire range of the observed joint distributions of S and δ. The $S-\delta$ relation could effectively discriminate among dust particle types. The observed S and δ values with the largest population density were best covered by models with $n > 2$, especially by those with n varying from 2.4 to 3.0.

Plain Language Summary Dust aerosols are irregularly shaped. Dust shape has a significant impact on the modeling of lidar observations. In this work, super-spheroid models (the conventional spheroid model is a special case) were used to study the impacts of nonsphericity and irregularity on lidar observations. In particular, we were interested in the lidar and depolarization ratios, because these ratios have proven useful for distinguishing among aerosol types in the atmosphere and will be measurable by the future Earth Cloud, Aerosol, and Radiation Explorer (EarthCARE) satellite. Because the lidar and depolarization ratios can be affected by multiple factors, including dust shape, refractive indices, and particle sizes, systematic theoretical studies related to these factors were conducted. Furthermore, we compared the theoretical simulations with NASA Langley airborne high spectral resolution lidar data, and found that super-spheroid models could be used to explain the wide variation of dust optical properties found in the lidar data. The present study confirmed that dust particles represented by super-spheroid models can be useful in lidar remote sensing applications. Based on this, the optimal parameters of super-spheroid models can be used to parameterize dust shapes.

1. Introduction

Dust, as one of the most important atmospheric aerosols (Tegen et al., 1997) exerts an enormous influence on both the climate and human health because of its large mass loading and wide spatial distribution. For example, exposure to fine particulate matter ($PM_{2.5}$), including dust, can harm human health by causing respiratory and cardiovascular diseases (Brunekreef & Holgate, 2002). Moreover, the transport of dust aerosols containing nutrients influences biogeochemical cycles on Earth, which could be a major factor in the variation of atmospheric carbon dioxide levels (Duce et al., 1991; Mahowald et al., 1999, 2005; Martin, 1990). Dust aerosols also affect the radiation budget of the Earth by directly influencing radiation absorption and scattering, and indirectly influencing liquid and ice clouds in the form of cloud condensation and ice nuclei, which fundamentally impact the lifetime of clouds and precipitation processes (Andreae & Rosenfeld, 2008; Kok et al., 2017; Levin et al., 1996; Mahowald et al., 2014).

Both remote sensing and radiative effect studies of dust aerosols rely on accurate characterization of the optical properties of dust particles. However, large uncertainties related to particle irregularity and refractive indices exist in estimations of the optical properties of dust, which complicates interpretations of remote sensing observations and assessments of dust radiative forcing in atmospheric models (Aoki et al., 2005; Bi et al., 2020;

Kok et al., 2017; Sokolik & Toon, 1999). Consequently, concerted efforts are being dedicated to investigating the optical properties, distribution, and transport of dust, and to developing appropriate models to improve remote sensing accuracy and the accuracy of climate models (Dentener et al., 1996; Di Biagio et al., 2014; Dubovik & King, 2000; Ginoux et al., 2001; Hess et al., 1998; Linke et al., 2006; Péré et al., 2018; Prospero et al., 2002; Rocha-Lima et al., 2018; Zender et al., 2003).

Global observation of aerosols has been performed by the Cloud–Aerosol Lidar with Orthogonal Polarization (CALIOP) lidar, which is a dual-wavelength polarization lidar onboard the Cloud–Aerosol Lidar and Infrared Pathfinder Satellite Observations (CALIPSO) satellite that has been operational since 2006 (Winker et al., 2010). Interpretation of lidar signals requires a theoretical understanding of the backscattering properties of such particles. The depolarization ratio (Kaufman et al., 2003; Nishizawa et al., 2007, 2011) contains important information about atmospheric particles, such as particle shapes, sizes, components, and refractive indices (Ansmann et al., 2005; Mishchenko & Sassen, 1998; Müller et al., 1999, 2007; Veselovskii et al., 2012). One effective approach for relating particle microphysics to particle optical properties is through laboratory experiments. However, in the context of lidar signals, it has been difficult to precisely characterize backscattering at 180°. For example, in the Amsterdam Light Scattering Database (Muñoz et al., 2012), the scattering matrices of dust aerosols at 441.6 and 632.8 nm have been measured in the scattering angle ranges of 3°–5° to 174°. Sakai et al. (2010) obtained dust depolarization ratios at scattering angles of 178.8°–179.6° at 532 nm. Järvinen et al. (2016) presented laboratory measurements of linear and circular near-backscattering depolarization ratios of dust at 488 and 552 nm wavelengths at 178°. Recently, depolarization ratios at the near-exact backscattering angle of 180° ± 0.2° were measured in the laboratory using Arizona Test Dust particles (Miffre et al., 2016). In Miffre et al. (2016), depolarization ratios up to 37.5% and 35.5% were obtained for sub-micron-size particles at wavelengths of 355 and 532 nm, respectively. Because CALIPSO has a conventional backscatter lidar, it provides an attenuated backscattering coefficient and the lidar ratio cannot be obtained directly. Aerosol classification and extinction retrieval from CALIOP are performed using either single wavelength (Omar et al., 2009; Kim et al., 2018) or dual wavelength (Nishizawa et al., 2011; Nishizawa, Okamoto, et al., 2008) data.

High spectral resolution lidar (HSRL) is a powerful technique that can independently measure the extinction and backscatter coefficients of aerosols and clouds, allowing the lidar ratio (defined as the extinction to backscatter ratio) to be obtained (Freudenthaler et al., 2009; Hair et al., 2008; Jin et al., 2020; Liu et al., 2002; Mona et al., 2012; Sroga et al., 1983). The lidar ratio and depolarization ratio relation is used to distinguish aerosol (Burton et al., 2012) and ice particle types (Okamoto et al., 2019, 2020). The Earth Cloud, Aerosol, and Radiation Explorer (EarthCARE) satellite is a joint venture between the European Space Agency (ESA) and Japanese Aerospace Exploration Agency (JAXA) scheduled for launch in 2023. Global cloud and aerosol profiles will be retrievable from the instruments on this satellite, including a 94-GHz cloud profiling radar with Doppler capability, Atmospheric Lidar (ATLID) instrument, multispectral imager, and a broadband radiometer (Nishizawa, Sugimoto, et al., 2008; Sato et al., 2009, 2018, 2019; Sato & Okamoto, 2011). ATLID is a 355-nm HSRL with a linear depolarization channel. The lidar ratio–depolarization ratio relations will be used for aerosol typing in conjunction with the EarthCARE level 2 aerosol-type product (Illingworth et al., 2015). Furthermore, extinction profiles for each aerosol component will be derived from ATLID, where a fixed shape is assumed for dust (Nishizawa, Sugimoto, et al., 2008). Advanced theoretical analysis of the lidar ratio–depolarization ratio with respect to dust shape, size, and refractive index is expected to facilitate the retrieval of dust microphysics at the wavelength of 355 nm, but this has not been fully investigated theoretically.

From a theoretical perspective, modeling nonspherical particles is a complex procedure because the optical equivalence between modeled and actual particles is not obvious. The use of spherical dust models obviously leads to error because of the zero depolarization. Extensive research on dust backscattering using spheroid models has been conducted (Dubovik et al., 2006; Mishchenko & Hovenier, 1995; Nishizawa et al., 2011; Veselovskii et al., 2010). A spatial Poisson-Voronoi tessellation was considered to model irregular mineral dust particles (Ishimoto et al., 2010). Gasteiger et al. (2011) simulated S and δ for six irregular dust models at four wavelengths of 355, 532, 710, and 1,064 nm for small and moderate particles. Saito and Yang (2021) investigated the shape and wavelength dependence of backscattering properties of dust by using 21 irregular hexahedral particles in a full aerosol size range. Furthermore, super-spheroids, which can model various particle shapes, have been proposed (Bi, Lin, Liu, & Zhang, 2018, Bin, Lin, Wang, et al., 2018). In recent studies, the scattering matrices of dust calculated with super-spheroids have been shown to have good consistency with those of the

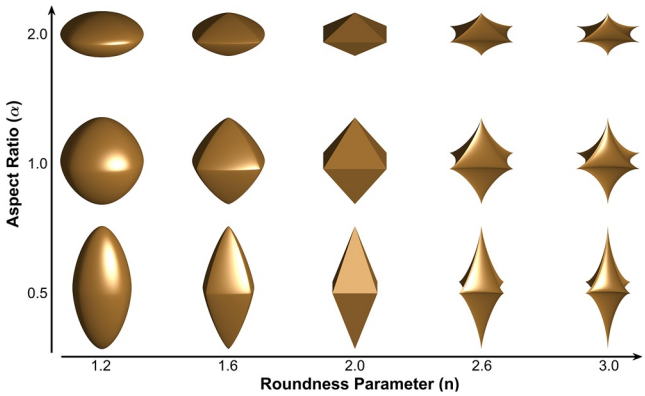

Figure 1. Super-spheroid models with different roundness parameters (n) and aspect ratios (α). Fifteen shapes ($n = 1.2$, 1.6, 2.0, 2.6, 3.0 and $\alpha = 0.5$, 1.0, 2.0) were selected for illustration.

Amsterdam–Granda databases (Lin et al., 2018), and have been tested against the polarized radiance measurements of the Polarization and Anisotropy of Reflectances for Atmospheric Sciences coupled with Observations from a Lidar (PARASOL) satellite (Lin et al., 2021). The depolarization properties of super-spheroids have been examined theoretically in relation to the complex refractive indices and shapes of atmospheric aerosols (Bi, Lin, Liu, & Zhang, 2018). Tang et al. (2019) investigated the effects of the morphology and absorptivity changes of soot-contaminated dust on lidar backscattering properties. However, a comprehensive survey of the variability of lidar ratio–depolarization ratio relationships produced by super-spheroid dust has not been performed over a wide range of dust shapes and sizes.

In this study, we systematically investigated the backscattering properties of dust at 355 nm over a wide range of particle shapes and effective sizes, by applying super-spheroids for the interpretation of future data from the EarthCARE ATLID. We aimed to assess, for the first time, the extent to which super-spheroids can reproduce the large variations observed in the joint distribution of the lidar ratio and depolarization ratio of HSRL observations for dust at 355 nm. To achieve this objective, the invariant imbedding T-matrix method (II-TM) (Bi et al., 2013; Bi & Yang, 2014) was employed for theoretical simulations. The ability to simulate the observed lidar ratio–depolarization ratio relationships using super-spheroid models was further investigated by analyzing dust observation data obtained from the National Aeronautics and Space Administration (NASA) Langley second-generation airborne High Spectral Resolution Lidar-2 (HSRL-2; Burton et al., 2015; Redemann et al., 2021).

The remainder of this paper is organized as follows. In Section 2, we describe the methodology and data. In Section 3, we comprehensively investigate the features of the lidar and depolarization ratios produced by super-spheroid models with various particle shapes, over a wide range of effective radii. Then, we compare the theoretical simulations with airborne HSRL observation data. Finally, we discuss the capability of super-spheroid dust models to account for the observed two-dimensional distribution of the lidar ratio and depolarization ratio at 355 nm. A summary and conclusion are provided in Section 4.

2. Methods and Data

2.1. Theoretical Procedures

The general equation of a super-ellipsoid can be written as follows (Barr, 1981):

$$\left[\left(\frac{x}{a}\right)^{2/e} + \left(\frac{y}{b}\right)^{2/e}\right]^{e/n} + \left[\frac{z}{c}\right]^{2/n} = 1, \tag{1}$$

where $a - c$ are the lengths of the three semi-major axes along the corresponding coordinate axes in the Cartesian coordinate system, and e and n are roundness parameters. Here, to reduce computation time and model complexity, we focus on the super-spheroidal model (where $e = n$ and $a = b$) obtained by the following equation:

$$\left(\frac{x}{a}\right)^{2/n} + \left(\frac{y}{a}\right)^{2/n} + \left(\frac{z}{c}\right)^{2/n} = 1. \tag{2}$$

As models with $n < 1$ are normally used to study cube-like sea salt aerosols (Bi, Lin, Wang, et al., 2018), we employed models with $1 < n \leq 3$ to study dust (Figure 1). The model with $n = 2$ is a standard octahedron. For models with $n < 2$, the particle shapes are convex. For models with $n > 2$, the shapes are concave. a/c is defined as the aspect ratio (α), and n is the roundness parameter. The size parameter is defined as kx_m, in which k is the modified wave number ($2\pi/\lambda$, λ is the wavelength) and x_m is the maximum of a and c, that is, the half maximum dimension.

Single particle optical properties were calculated by the II-TM method, as described by Bi et al. (2013) and Bi and Yang (2014), to ensure an acceptable computation time for relatively large kx_m range (0.1–50 for this study).

Table 1
The Parameters of the Super-Spheroid Dust Models Used in This Study

Purpose	Computational Method	Size parameter (kx_m)	Aspect ratio (α)	Roundness parameter (n)	Refractive index	
					Real part (m_r)	Imaginary part (m_i)
Simulate dust particles	II-TM	0.1–50	0.5, 0.6, 0.7, 0.8, 0.9, 1.0, 1.2, 1.4 1.6, 1.8, 2.0	1.2, 1.4, 1.6, 1.8, 2.0, 2.2, 2.4, 2.6, 2.8, 3.0	1.50	0.003
Test the uncertainty		0.1–50	0.5, 0.6, 0.7, 0.8, 0.9, 1.0, 1.2, 1.4 1.6, 1.8, 2.0	1.2, 1.4, 1.6, 1.8, 2.0, 2.2, 2.4, 2.6, 2.8, 3.0	1.50	0.001, 0.005, 0.008
		0.1–100	0.5, 1.0, 2.0	2.6, 2.8, 3.0	1.50	0.001, 0.005
	IGOM	100–1,000	1.0	2.8	1.50	0.001, 0.005

Note. In the II-TM simulations, the step intervals of size parameters were 0.1, 0.2, 0.5, 1, 2, 5, 10 in the range of 0.1–10, 10–20, 20–30, 30–40, 40–50, 50–60, 60–100, respectively. In the IGOM simulations, the step intervals of size parameters were 5 and 10 in the range of 100–200 and 200–1,000, respectively.

For a few selected models (Table 1), the maximum size parameter was extended to 100 to perform sensitivity analysis. Besides, the results calculated by the improved geometric optical method (IGOM; Bi & Yang, 2017; Yang & Liou, 1996) were also considered to investigate the lidar ratio–depolarization ratio relationships produced by large super-spheroid dust up to $kx_m = 1{,}000$ as a reference. The parameters used in this study are listed in Table 1. The refractive index $m_r + i \cdot m_i$ of dust at a wavelength of 355 nm was set to $1.50 + 0.003i$ according to Di Biagio et al. (2019). Large uncertainty exists, especially for the imaginary part, in refractive indices of mineral dust in the shortwave spectral range (Di Biagio et al., 2019; Dubovik et al., 2002; Haywood et al., 2003; Müller et al., 2009, 2011; Patterson et al., 1977; Shettle & Fenn, 1979; Wagner et al., 2012). Most recent studies indicated that dust particles can be weakly absorptive (Di Biagio et al., 2019; Zong et al., 2021). The sensitivity of the results to m_i was discussed in Section 3.

The scattering matrix represents how the polarization state of the scattered light changes relative to the original incident light beam. For this study, we considered an ensemble of randomly oriented super-spheroidal particles, for which the scattering matrix is written as follows:

$$\begin{bmatrix} P_{11}(\theta) & P_{12}(\theta) & 0 & 0 \\ P_{12}(\theta) & P_{22}(\theta) & 0 & 0 \\ 0 & 0 & P_{33}(\theta) & P_{34}(\theta) \\ 0 & \mathbf{0} & -P_{34}(\theta) & P_{44}(\theta) \end{bmatrix}. \tag{3}$$

In the above, θ denotes the scattering angle. Considering the size distribution of particles $\frac{dN}{dr}$, the bulk scattering matrix elements $\langle P_{ij} \rangle$ are expressed as follows:

$$\langle P_{ij} \rangle = \frac{\int_{r_{\min}}^{r_{\max}} P_{ij}(r) C_{\text{sca}}(r) \frac{dN}{dr} dr}{\int_{r_{\min}}^{r_{\max}} C_{\text{sca}}(r) \frac{dN}{dr} dr}, \tag{4}$$

in which P_{ij} denotes an arbitrary element of the scattering matrix in Equation 3. $C_{\text{sca}}(r)$ is the particle scattering cross section, and r is the geometric radius of a sphere having the same volume as the actual particle (i.e., volume-equivalent sphere radius). In this study, the log-normal size distribution was used. It can be expressed as below:

$$\frac{dN}{dr} = \frac{N_0}{r\sqrt{2\pi} ln\sigma_g} \text{Exp}\left[-\frac{(lnr - ln\mu_g)^2}{2(ln\sigma_g)^2}\right], \tag{5}$$

in which N_0 is the total number of an ensemble of particles, σ_g denotes the geometric standard deviation, and μ_g is the geometric mean. The value of N_0 is irrelevant in this study and was assumed to be 1 μm^{-3}. The σ_g reported

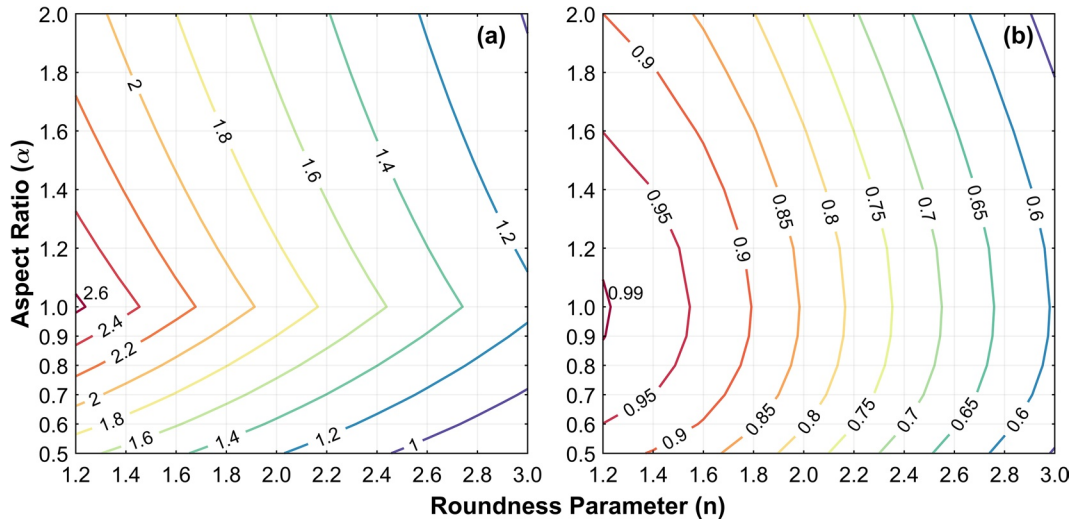

Figure 2. The maximum volume equivalent sphere radius r_{max} (unit:μm) at a wavelength of 355 nm corresponding to the size parameter of $kx_m = 50$ (a) and the ratio of two different effective radii (R/r_{eff}) (b) for super-spheroid models with different roundness parameters (n) and aspect ratios (α). The maximum dimension of the super spheroids at $kx_m = 50$ is 5.65 μm.

in the literature is within the range of 1.6–2.4 , and the majority of values are concentrated within 1.8–2.2 (Hess et al., 1998; Mahowald et al., 2014; Reid, Reid, et al., 2003). A typical value for dust of $\sigma_g = 2.0$ (Reid, Jonsson, et al., 2003) was found to produce visible optical depth in good agreement with satellite observations (Schulz et al., 1998). Therefore, we focused on the result where $\sigma_g = 2.0$, and $\sigma_g = 1.6$, 1.8, and 2.2 were used for the sensitivity study. r_{min} and r_{max} are the minimum and maximum volume-equivalent sphere radius corresponding to $kx_m = 0.1$ and 50, respectively, and μ_g varied within the range $[r_{\text{min}}, r_{\text{max}}]$. Figure 2a shows r_{max} of super-spheroid models with different n and α corresponding to $kx_m = 50$. The maximum dimension of the super-spheroids at $kx_m = 50$ is 5.65 μm. The effect of r_{max} choice on the accuracy of bulk optical properties will be discussed in Section 3.4. Lidar observables can be obtained from Equations 3–5. For linear polarized incident light and a scattering angle of 180° (π), $P_{12}(\pi)$ is zero, and the depolarization ratio (δ) can be obtained using Equation 6:

$$\delta = \frac{1 - \langle P_{22}(\pi)\rangle / \langle P_{11}(\pi)\rangle}{1 + \langle P_{22}(\pi)\rangle / \langle P_{11}(\pi)\rangle}. \tag{6}$$

The lidar ratio is the ratio between the backscattering (β_λ) and extinction ($\sigma_{\text{ext},\lambda}$) coefficients, and is given as follows:

$$S_\lambda = \frac{\sigma_{\text{ext},\lambda}}{\beta_\lambda}, \tag{7}$$

where

$$\beta_\lambda = \frac{1}{4\pi} \int_{r_{\text{min}}}^{r_{\text{max}}} P_{11,\pi,\lambda} C_{\text{sca},\lambda}(r) \frac{dN}{dr} dr, \tag{8}$$

$$\sigma_{\text{ext},\lambda} = \int_{r_{\text{min}}}^{r_{\text{max}}} C_{\text{ext},\lambda}(r) \frac{dN}{dr} dr. \tag{9}$$

$C_{\text{ext},\lambda}$ denotes the particle extinction cross section, and λ is the wavelength of the incident light. In the following, $\lambda = 355$ nm, and we omit the wavelength subscripts. The size of an ensemble of dust is described by the effective radius (r_{eff}), which can be calculated via the following definition (Hansen, 1971):

$$r_{\text{eff}} = \frac{\int_{r_{\text{min}}}^{r_{\text{max}}} r^3 \frac{dN}{dr} dr}{\int_{r_{\text{min}}}^{r_{\text{max}}} r^2 \frac{dN}{dr} dr}. \tag{10}$$

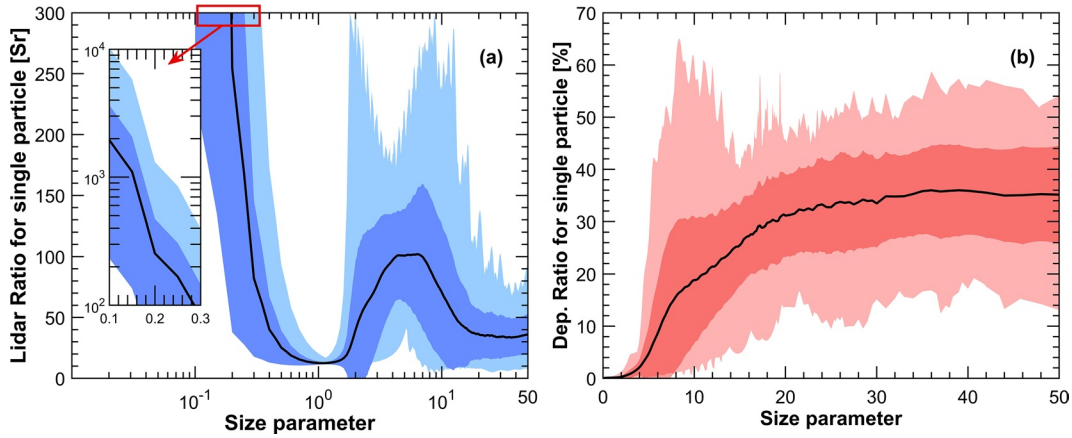

Figure 3. Lidar ratio (a) and depolarization ratio (b) for single particle as a function of size parameter kx_m for all particles in the first row of Table 1. Models with a maximum size parameter of 50 are included, and the wavelength is 355 nm. The black line is the average of all models. The light-blue and light-red areas in (a and b), respectively, show the variation range of lidar ratio and depolarization ratio. The dark-blue and dark-red areas in (a and b), refer to the standard deviation of lidar ratio and depolarization ratio.

For nonspherical particles, another definition of effective radius (referred as R here) given in Equation 11 is also often used (Hansen & Travis, 1974).

$$R = \frac{3\int_{r_{\min}}^{r_{\max}} V \frac{dN}{dr} dr}{4\int_{r_{\min}}^{r_{\max}} \bar{A} \frac{dN}{dr} dr}, \tag{11}$$

where V is the volume and $\bar{A}$ is the averaged projected area of an individual particle. In the following texts, we used Equation 10 for data analysis. However, the ratios of the aforementioned two effective radii at different shape parameters are shown in Figure 2b.

Figure 3 illustrates the variability of the simulated S and δ at $\lambda = 355$ nm for an individual particle before the size integration of all super-spheroid models listed in Table 1. The S and δ variabilities were large, indicating a large probability to reproduce various observations using the super-spheroid models. In this sense, the present models show potential superiority for simulating dust particles. The lidar ratio produced by different models ranged from about 10 Sr to more than 150 Sr at size parameters >~0.2. Most of the δ are smaller than 45%, although some of them exceed 50%.

2.2. Airborne High Spectral Resolution Lidar Observations

Dust events observed by the NASA Langley second-generation airborne HSRL-2 during the Deriving Information on Surface Conditions from Column and Vertically Resolved Observations Relevant to Air Quality (DISCOVER-AQ) project (Burton et al., 2015) and the ObseRvations of Aerosols above CLouds and their intEractionS-3 (ORACLES-3) campaign (Redemann et al., 2021) were used in this study. Details of the observations are provided in Section 3.

3. Results: Lidar Ratio–Depolarization Ratio Relations of Atmospheric Dust Aerosols

First, we explore the shape (roundness parameter, aspect ratio) dependence of optical properties ($S, \delta, \sigma_{\text{ext}}, \beta$) at a wavelength of 355 nm. Next, we investigate the r_{eff} dependences of S and δ. Then, the lidar and depolarization ratio relations for super-spheroid models are examined.

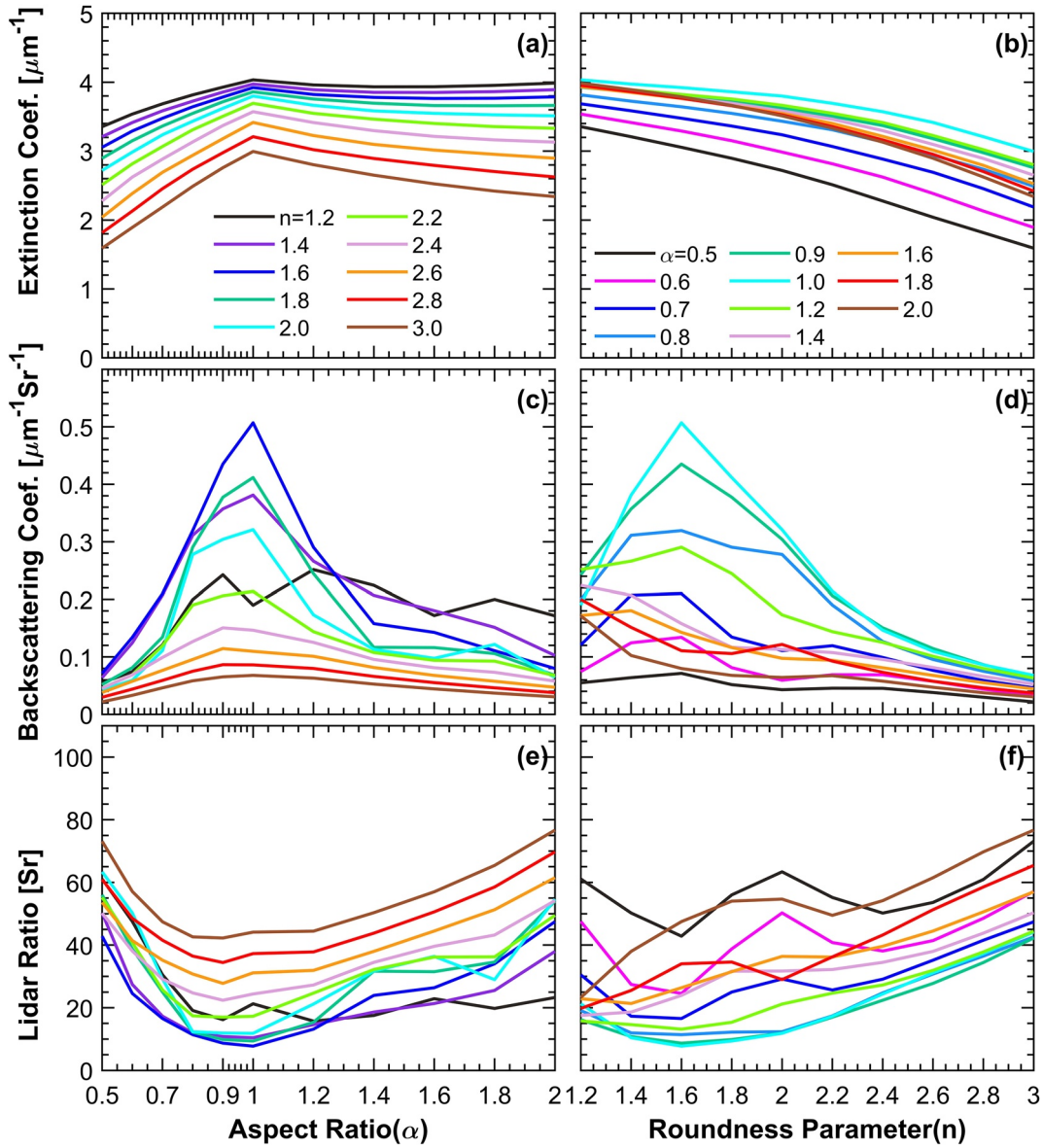

Figure 4. Extinction coefficient (σ_{ext}), backscattering coefficient (β), and lidar ratio (S) at a wavelength of 355 nm as functions of the aspect ratio (α) and roundness parameter (n). $\mu_g = 0.5$ μm was assumed.

3.1. Effects of the Shape Parameters on the Backscattering Properties of Super-Spheroid Models

The dependences of σ_{ext} and β on the shape parameters (n, α) were determined, as shown in Figures 4a and 4b, to facilitate understanding of the features seen in S (Figures 4e and 4f). The geometric mean radius $\mu_g = 0.5$ μm was assumed.

As shown in Figure 4b, σ_{ext} decreased with an increase of the roundness parameter (n). β generally showed a similar trend but with a steeper rate of decrease with n. Overall, S increased with n. Both σ_{ext} and β reached a peak at $\alpha = 1$ and decreased as α deviated from 1.0 (Figures 4a and 4c). The variation of σ_{ext} due to α remained relatively small particularly when $\alpha > 1$ (Figure 4a). The differences in σ_{ext} for the same α or n were within a factor of 2 (see Figures 4a and 4b). However, β changed dramatically with α and n. For example, the maximum differences in β for the same α or n exceeded one order of magnitude. Related to the ratio of σ_{ext} and β, S was lowest at α close to 1 (range: 0.8–1.2) and increased as α deviated from 1.0. Both large n and deviation of α from 1.0 tend to produce large S values.

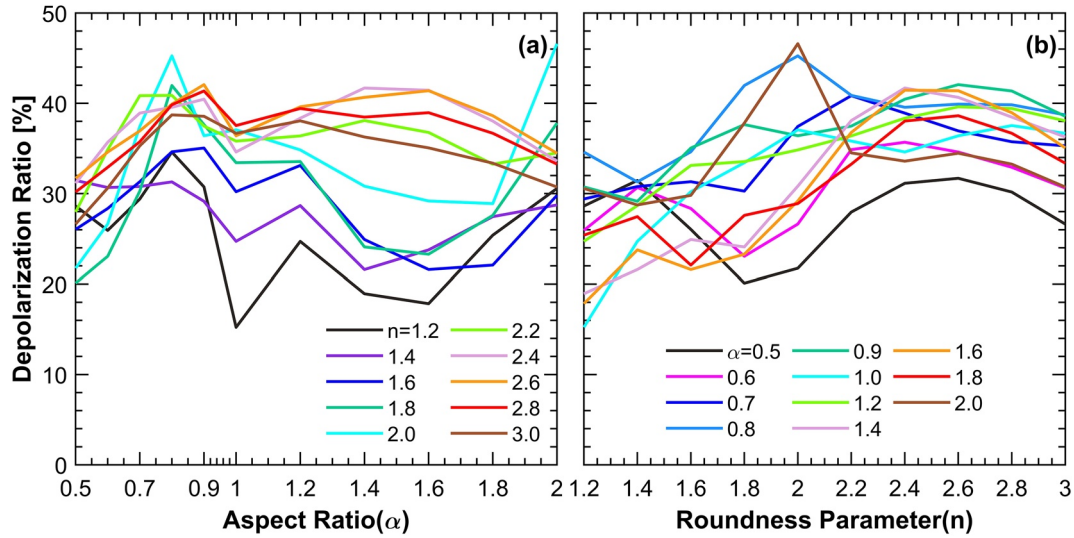

Figure 5. Similar to Figures 4e and 4f, but representing the depolarization ratio (δ).

Figure 5 shows the dependence of the depolarization ratio (δ) on the aspect ratio (α) and roundness parameter (n). In Figure 5a, the δ values of super-spheroid models are mainly concentrated in the range from 20% to 40%. Generally, models with $n > 2$ produced larger δ values than models with $n < 2$. Models with $n > 2$ seemed to show less variability in δ due to α compared to models with $n \leq 2$ for the size considered. Most of the models showed a local minimum in δ at $\alpha = 1.0$.

3.2. Dependence of the Lidar Ratio and Depolarization Ratio on r_{eff}

Figures 6 and 7 show the r_{eff} dependence of the lidar and depolarization ratios for super-spheroid models. δ values for models with different n are shown in Figure 6b. Generally, δ depends on r_{eff} and shape, but the r_{eff} dependence is considered to weaken as r_{eff} approaches the geometric optics region. The effective size range depends on n and α. For models with $n > 2$, δ was largely dependent on r_{eff} and increased with r_{eff} to about 40% in the size range considered. The variability in δ due to α became relatively small for $n \geq 2.4$. Similarly, the variability in δ due to n was found to be small among the models with $n \geq 2.4$ (Figure 6a). For models with $n \leq 2$, δ increased with r_{eff}, and generally showed a weaker dependence on r_{eff} at $r_{eff} > 0.4$ μm and $r_{eff} > 1$ μm for α close to 1. For $n \leq 2$, the maximum δ produced by the models largely depended on α (Figure 6b) and n (Figure 6a). In Figure 7, lidar ratio S peaked at around $r_{eff} = 0.1$–0.2 µm and then decreased to a lower value. Note that some models with a small n showed a rebound of S at a large r_{eff}. This phenomenon was fundamentally related to the fact that the absorption became obvious when the particle size was large. The S values of the models will show a dramatic increasing trend at larger sizes for relatively high m_i. As shown in Figure 4, S generally increased with n (Figure 7a), and the S values were smallest for models with α near 1 and largest for those with α deviating from 1.

3.3. Lidar Ratio (S)–Depolarization Ratio (δ) Relations of Super-Spheroid Models and Airborne HSRL Observations

To assess the capability of super-spheroid dust to simulate the two-dimensional distribution of S and δ observed at 355 nm, two dust events observed by the NASA Langley HSRL-2 at 355 nm were investigated in this study. The first dust event was observed in the Midwest USA on 13 July 2014, during the DISCOVER-AQ campaign (Figures 8a–8d), and the second one was observed over the western Atlantic Ocean, during the ORACLES-3 campaign on 21 September 2018 (Figures 8e–8h). The observation in 2014 revealed a dust layer around the altitude of 2 km (Burton et al., 2015), and the observation in 2018 indicated a lower dust layer between about 1 and 3 km. The majority of the S values observed by the airborne HSRL varied between 40 and 60 Sr (Figure 9a). Typically reported values of S for dust in the East Asian and Middle Eastern desert regions are in the range of 30–50 Sr (Filioglou et al., 2020; Hofer et al., 2017, 2020; Mamouri et al., 2013; Noh et al., 2008), whereas the values of 40–65 Sr are more representative of Saharan regions (Groß et al., 2011, 2015; Mattis et al., 2002; Papayannis

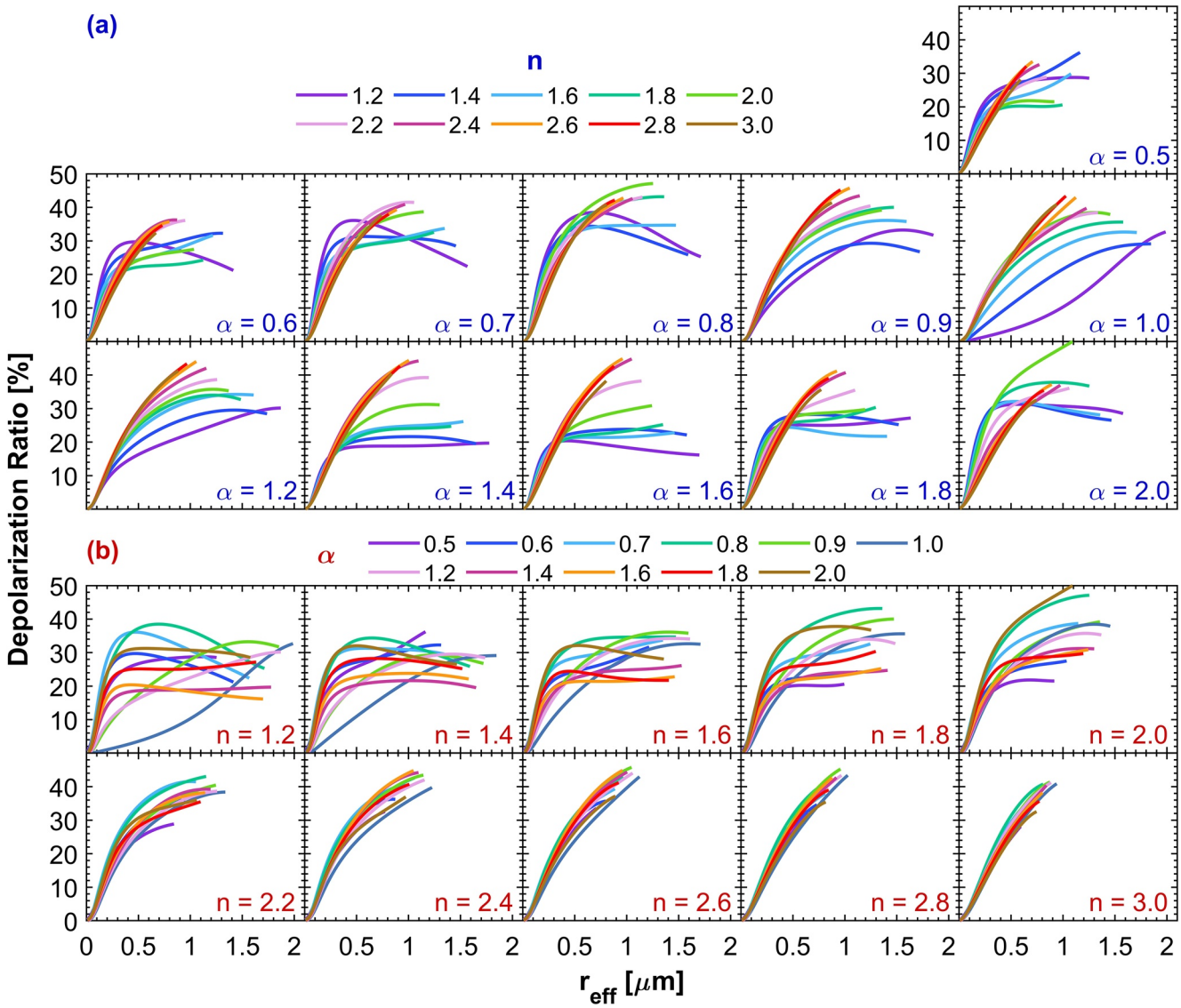

Figure 6. δ for different super-spheroid models with α fixed (a) and n fixed (b) as a function of r_{eff}. α varies from 0.5 to 2.0 for each subplot in (a) and n varies from 1.2 to 3.0 for each subplot in (b). The wavelength was 355 nm.

et al., 2005; Preiβler et al., 2011; Tesche et al., 2009; Veselovskii et al., 2016; Wiegner et al., 2011). The measured δ were mostly within the range for dust (20%–40%) reported in other studies (Burton et al., 2015; Freudenthaler et al., 2009; Groβ et al., 2011; Haarig et al., 2017; Mamouri & Ansmann, 2017; Wiegner et al., 2011). The maximum δ at 355 nm in the 2014 measurements was approximately 28%, whereas the 2018 observation showed a much higher δ in the dust layer of up to about more than 45%. In this study, we considered cloud-screened aerosol data at 355 nm, and further screened out data with depolarization ratio (532 nm) <25% (Burton et al., 2015) as well as aerosols below 0.5 km to minimize the effect of non-dust aerosols. By using the method of Sugimoto and Lee (2006), we calculated the dust mixing ratio (i.e., the contribution of dust to 532 nm backscattering) and the result showed that dust aerosols accounted for more than 90% and 80% in the 2014 and 2018 observations, respectively. That means, the two observational cases were dust-dominated. Figure 8 shows the measurement curtain of the lidar observables reported at 10 s time interval and 15 m vertical resolution.

The $S-\delta$ relation produced by the super-spheroid models exhibited a wide variation (Figure 9a). As illustrated, the $S-\delta$ domains of the HRSL measurements were well-covered by the super-spheroid models. A small portion of the δ observed at the edge of the dust layer was larger than 40% (see Figure 8g), and this portion was not

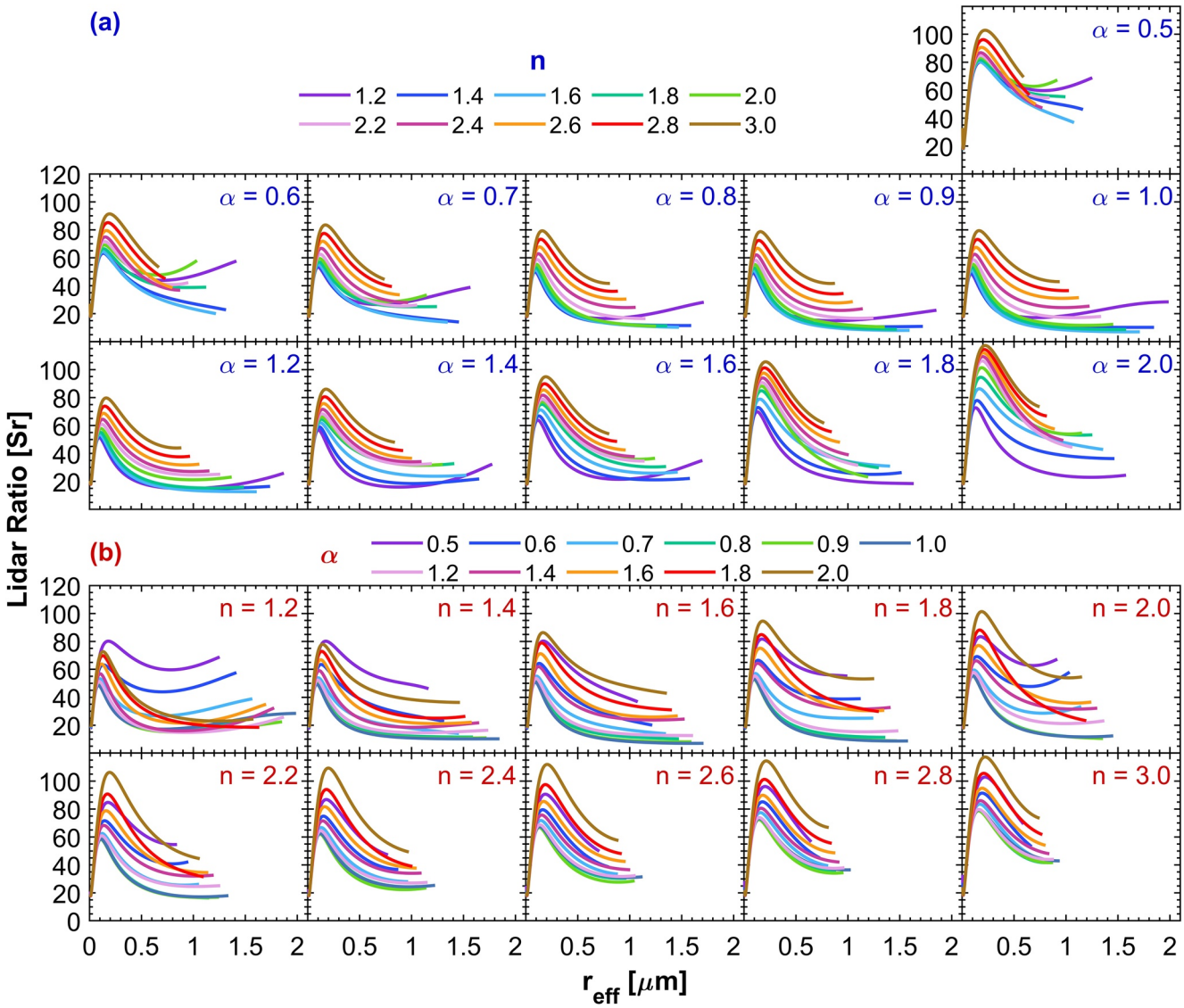

Figure 7. Similar to Figure 6, but for lidar ratio S.

reproduced well by the models in the size range considered. Despite this, the super-spheroid models were typically capable of simulating the observed $S-\delta$ range of dust obtained from the HSRL at 355 nm.

Figures 9b–9k show the $S-\delta$ relations for 10 groups of super-spheroid models, respectively. For each group, the results of super-spheroid models with the same roundness parameter but different aspect ratios are presented. Compact models denote shapes with the aspect ratio close to unity ($\alpha \geq 0.8$ and $\alpha \leq 1.2$), whereas extreme models indicate particles with the aspect ratio deviating from unity (hereafter, extreme α), that is, $\alpha = 0.5$, 0.6, 0.7, 1.4, 1.6, 1.8, and 2.0. The δ and S showed different features among the models with $n > 2$ and $n < 2$, as well as those with α near 1 and extreme α. Generally, the simulated S values decreased with increasing δ values at $\delta > 10\%$ in all models, but a weaker dependence of S on δ was seen for the models with $n < 2$ and extreme α. These models implied that dust with a large size had a relatively small δ, which could be unrealistic for modeling dust near source regions. The observed two-dimensional distributions of S and δ with moderate S (30–70 Sr) and δ (20%–40%) values, which had the largest population density, were best covered by the models with $n > 2$, and especially by considering those with n varying from 2.4 to 3.0. Considering the models with $n =$ 2.4–3.0, the measurements in 2014 implied that the r_{eff} of dust particles mostly fell into the range of 0.2–0.6 μm, while a portion of the measurements in 2018 indicated that dust particles could be larger than 0.8 μm. The

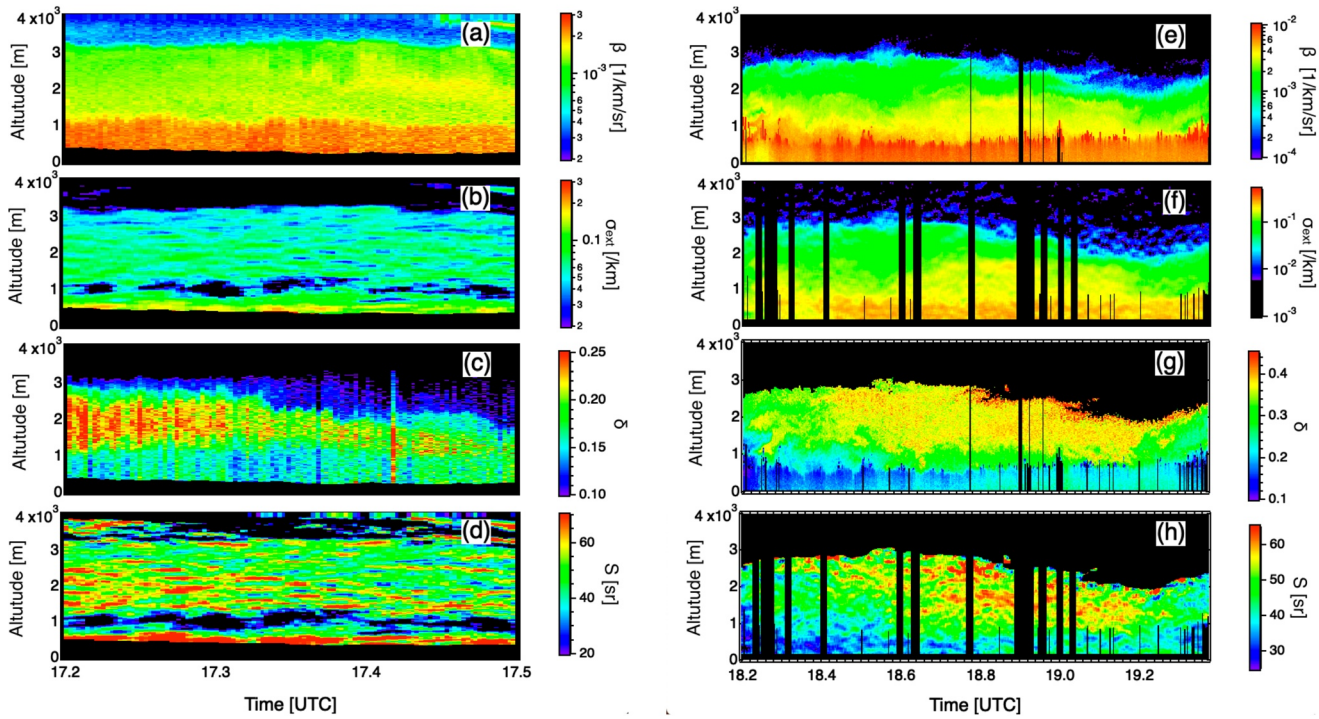

Figure 8. Measurement curtain of the (a and e) particle backscatter coefficient, (b and f) aerosol extinction coefficient, (c and g) aerosol depolarization ratio, and (d and h) lidar ratio at 355 nm obtained from the HSRL-2 instrument. (a–d) and (e–h) correspond to the observations in the Midwest USA (from 36.1°N 91.1°W to 39.5°N 102.6°W), on 13 July 2014, and from Delaware in the U.S. to South America (from 37.9°N 75.5°W to 14.3°N 60.2°W) on 21 September 2018, respectively.

positive correlations of S and δ in lidar measurements might imply that the dust particles have various size and shapes. However, a mixture with a small portion of other aerosols such as sea salt aerosols could also contribute to this phenomenon.

For comparison purposes, we included the result of the Texas A&M University Comprehensive Dust Scattering (TAMUdust2020) Database model 3 in Saito and Yang (2021) in Figure 9, which was shown to be optimal in simulating dust backscattering properties. The model 3 (severely irregular model) of TAMUdust2020 slightly overestimated S of the measurements. Interestingly, for the range of $\delta = 20\%$–40%, the TAMUdust2020 model was similar to the present super-spheroid models with large n (e.g., $n = 2.8$ and 3.0), and implied similar r_{eff} values for the range of $\delta = 22\%$–36%. The S and δ relation for large dust sizes ($r_{\text{eff}} > 2.0$ μm) in the TAMUdust2020 model showed dramatic rising trend in S, which was out of the S–δ range reported from the observation data used in this study.

A portion of the region with $\delta < 30\%$ was also explainable by models with $n < 2$ and extreme α. For example, models with $n = 2.8$, $\alpha = 1.0$ and $n = 1.6$, $\alpha = 1.8$ produced similar S (=50 Sr) and δ (= 25%) values at $r_{\text{eff}} = 0.5$ μm (Figures 6 and 7). Additional information, such as observations at different wavelengths, may provide an effective method for further investigating the differences among the models at $\delta < 30\%$. In other S–δ regions of the observed two-dimensional histogram, results with small S (<30 Sr) and δ (<20%) values were explainable by compact particles with α near 1 and $n < 2$. A small proportion of the observations showed large δ (>40%) values at $S > 60$ Sr, and these were partly explained by a model having an extreme α at $n = 2.0$ for the size range considered. The region with $S > 60$ Sr and small δ (<25%) values was explainable by all categories of n. The r_{eff} had a relatively small dependence on shape when $\delta < 20\%$–25% and may be well inferred in this δ range (Figure 6a).

Note that the models with $n = 1.2$, 1.4, which were almost spheroid, were not sufficient to account for the measurements with larger δ values. In this regard, super-spheroid models with relatively large n were superior to spheroid-like models ($n = 1.2$, 1.4) and spheroid models ($n = 1.0$) for simulating the large variation of S and δ of atmospheric dust.

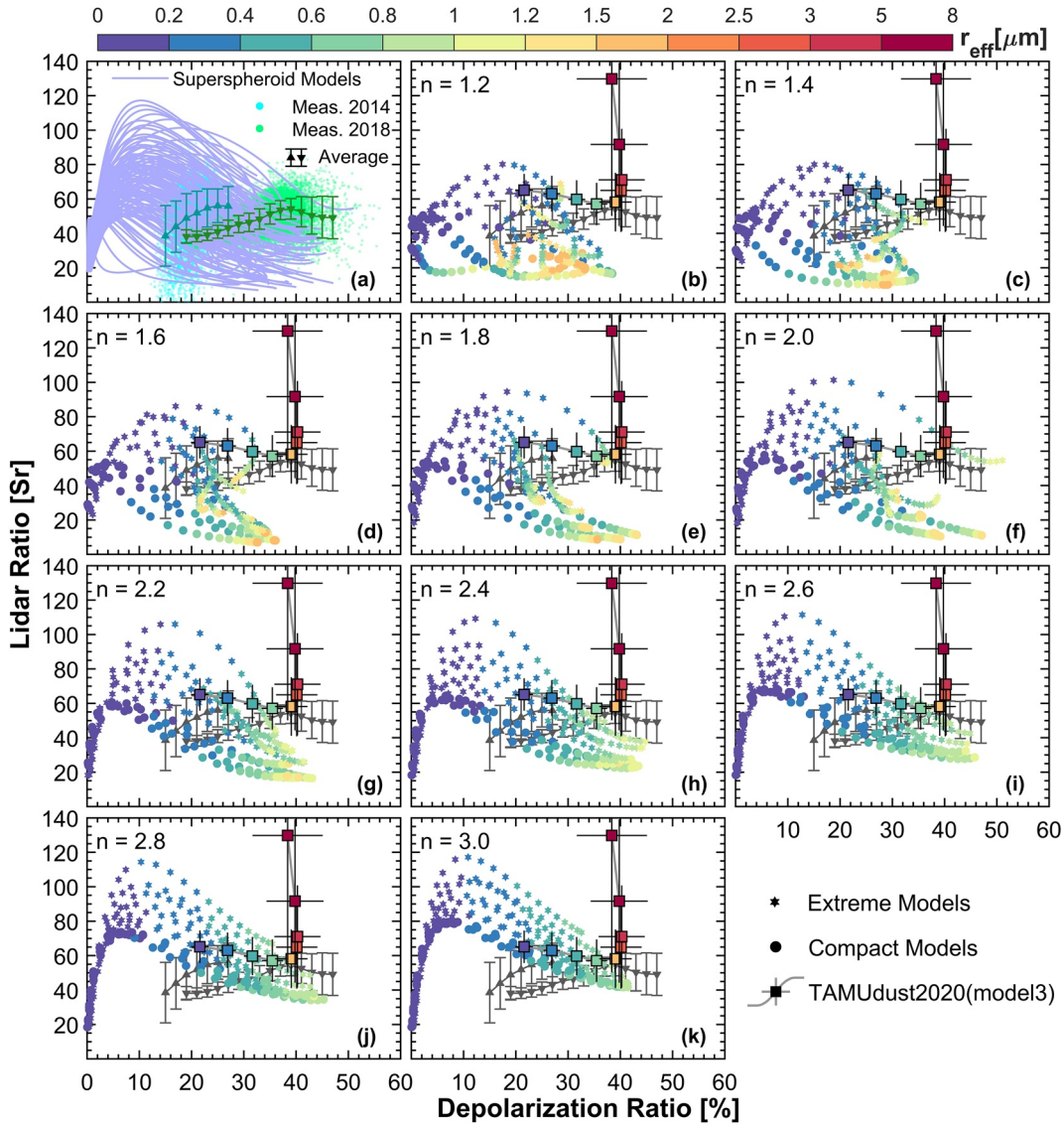

Figure 9. Comparisons of $S-\delta$ relations obtained from the HSRL-2 at a wavelength of 355 nm and their counterparts simulated using the super-spheroid models. (a) Shows the results of all super-spheroid models and the observation data. The cyan scatters show the scatter plot of the lidar data obtained on 13 July 2014 while the green ones show those obtained on 21 September 2018 (the time interval was 10 s and the vertical resolution was 15 m). The upward-triangle and downward-triangle with bars refer to the mean and standard deviation of lidar ratio in each depolarization-ratio bin. (b–k) Show the results of 10 groups of super-spheroids. In each group, the roundness parameter is the same (indicated in the subplot), but the aspect ratio (α) varies from 0.5 to 2.0. Compact models with $0.8 \leq \alpha \leq 1.2$ and extreme models with $\alpha > 1.2$ or $\alpha < 0.8$ are shown with circles and solid stars, respectively. The colors of stars and circles represent the r_{eff} of the models at 25 discrete sizes (see the color bar on the top of panel). The square symbols with bars represent the model three in Saito and Yang (2021), which remains the same in (b–k). Note, the definition of r_{eff} in Equation 10 was applied to the TAMUdust2020 model 3.

Figure 10 further summarizes the $S-\delta$ relationship produced in four different super-spheroid categories: (1) $n < 2$ and α near 1; (2) $n < 2$ and extreme α; (3) $n \geq 2$ and α near 1; and (4) $n \geq 2$ and extreme α. Larger S values in the observation were better modeled by super-spheroids with extreme α. Larger δ values were better modeled by super-spheroids with $n \geq 2$. It is apparent that most of the observed δ range could be explained by super-spheroid models with different sets of n and α. Category 1 could explain the observed S–δ relation when $S < 30$ Sr and $\delta < 20\%$. Category 2 could explain those when $\delta < 30\%$. Categories 3 and 4 could produce a wider

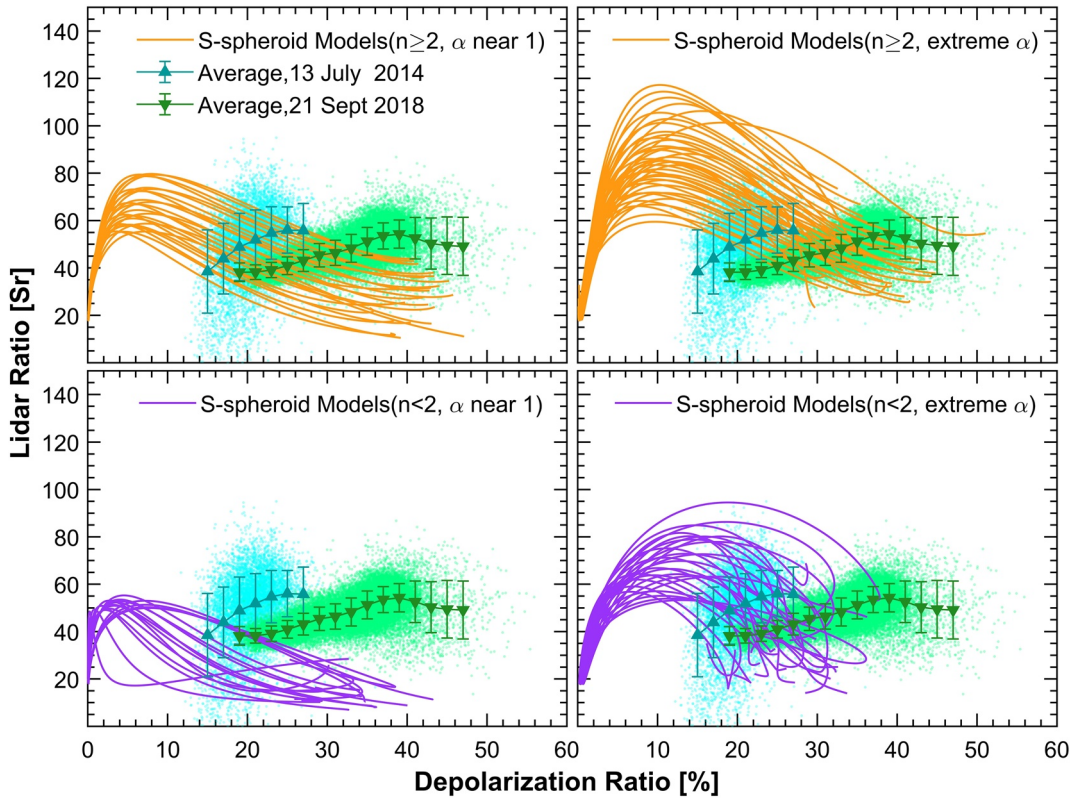

Figure 10. $S-\delta$ relations for the super-spheroid models and observations for the four categories at a wavelength of 355 nm.

range of S–δ values and were representative of the majority of the observation data, which had moderate S and δ values.

3.4. Discussion

The standard deviation σ_g and complex refractive index can affect $S-\delta$ relations. The σ_g chosen in the study was 2.0, which was regarded as typical for dust, and the refractive index was set to 1.50 + 0.003i at a wavelength of 355 nm. However, both of these were influenced by the source region of the dust, as well as the altitude and lifetime in the atmosphere. The measurements on 13 July 2014 were conducted in the Midwest USA, but the back-trajectories indicated that the dust layer was probably transported over a long period of time from the Sahara (Burton et al., 2015). The measurements on 21 September 2018 were conducted over the western Atlantic Ocean, and showed a relatively lower dust layer in altitude and higher δ values. The observed dust could be transported from North Africa according to the Hybrid Single-Particle Lagrangian Integrated Trajectory model (HYSPLIT; Rolph et al., 2017; Stein et al., 2015).

Figure 11 shows the σ_g dependence on $S-\delta$ relationships of super-spheroid models. The difference in S for a given δ between models with $\sigma_g = 1.8$, 2.0, and 2.2 was nonsignificant. The difference between $\sigma_g = 1.8$ and 2.2 was about 10%, meaning that σ_g variation in the reported range had little influence on the major findings of this study.

The lidar ratio is sensitive to dust absorption. Thus, S is significantly influenced by the imaginary part of the refractive index (m_i), which is related to the mineralogical composition that varies among different regions (Kim et al., 2020; Mamouri et al., 2013; Nisantzi et al., 2015; Shi et al., 2005; Shin et al., 2018; Veselovskii et al., 2020). The depolarization ratio δ is also affected by particle absorption, although less strongly. Figure 12 shows the influence of m_i on the δ, S and $S-\delta$ relations for models with $n = 2.8$ and $\alpha =$ 1.0. As shown in Figures 12a and 12b, δ increased as m_i decreased, while S increased with m_i.

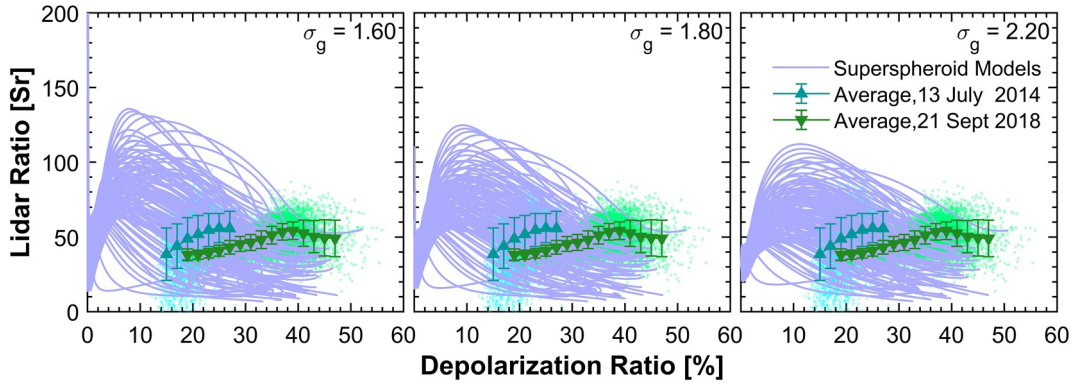

Figure 11. σ_g dependence on $S-\delta$ relationships of super-spheroid models at a wavelength of 355 nm. The σ_g values chosen are 1.6, 1.8, and 2.2.

Figure 12c shows that the difference between models with $m_i = 0.001$ and $m_i = 0.003$ was nonsignificant, while the difference for models with $m_i = 0.005$ and 0.008 was large, and S increased with m_i for the same δ. As the observations might have a Saharan origin, $m_i = 0.008$ could be too high according to the imaginary part of the refractive index, that is, [0.002, 0.003], reported at a wavelength of 355 nm by Stegmann and Yang (2017); and the mean measurement value of 0.0033 at a wavelength of 370 nm noted by Di Biagio et al. (2019) might be appropriate. Regarding $0.001 < m_i < 0.005$, the simulated S mostly increases by about 0%–50%, depending on δ, and models with $n = 2.4$–3.0 and α with values near 1 are expected to produce suitable optical properties at larger δ values matching the majority of the HSRL-2 observations (Figure 9). These models have also shown good performance with respect to producing the scattering matrices of dust obtained by laboratory measurements at proximal

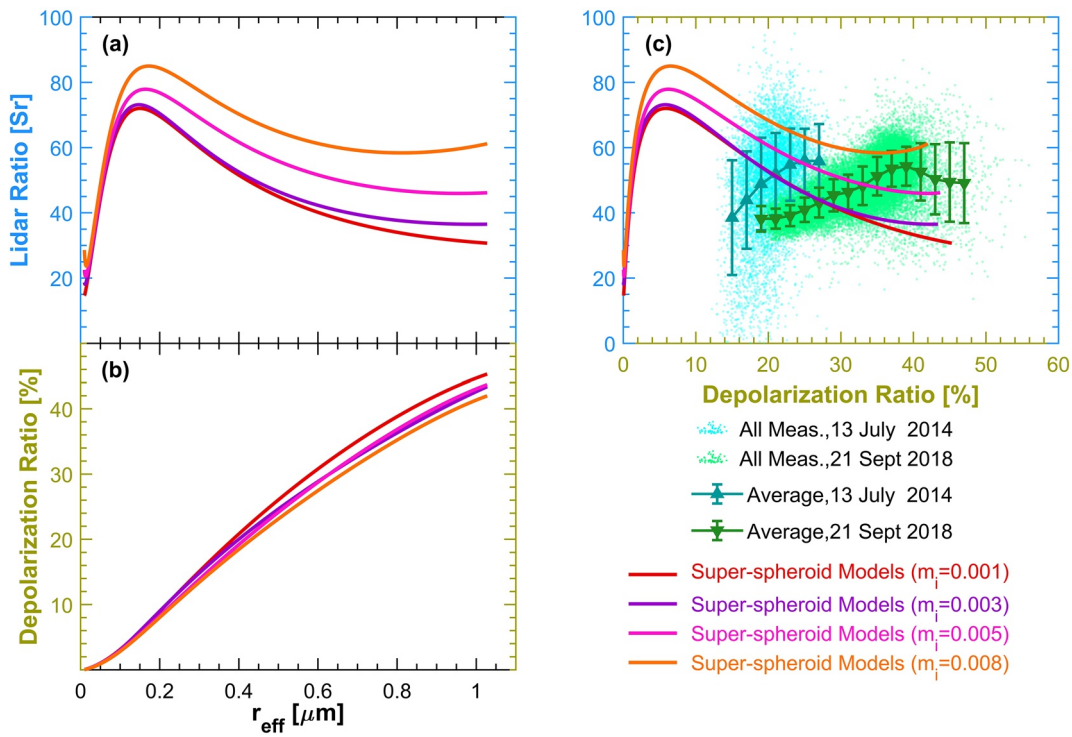

Figure 12. Lidar ratio S (a) and depolarization ratio δ (b) as a function of r_{eff}, and the $S-\delta$ (c) relationships for the super-spheroid model with roundness parameter $n = 2.8$ and aspect ratio $\alpha = 1.0$. Four imaginary parts of the refractive index (m_i) at a wavelength of 355 nm are considered. The real part of the refractive index is 1.5, and the maximum size parameter is 50.

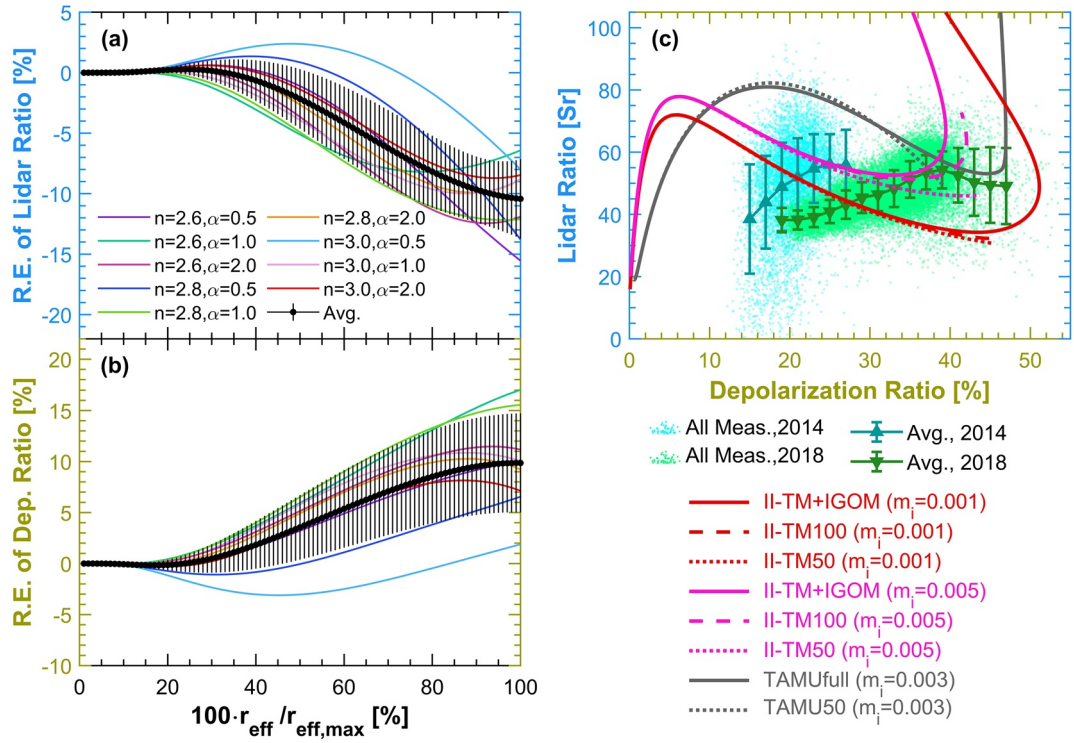

Figure 13. The relative error (R.E.) of lidar ratio S (a) and depolarization ratio δ (b) obtained by II-TM50 in respect to II-TM100 for the same r_{eff}. The horizontal axis shows the ratio of the r_{eff} value to the $r_{\text{eff,max}}$ value for each super-spheroid models ($100r_{\text{eff}}/r_{\text{eff,max}}$). The super-spheroid models with $n = 2.6$, 2.8, 3.0 and $\alpha = 0.5$, 1.0, 2.0 were employed and indicated by color lines. For each model, the average result for two different refractive indices ($1.50 + 0.001i$ and $1.50 + 0.005i$) are shown. The average and standard deviation of the errors of all models at the same horizontal axis value is shown with black lines and symbols for S and δ in (a and b). The S–δ relations (c) computed with different maximum size parameters ($kx_m = 50$, 100 and 1,000) for super-spheroid model with $n = 2.8$ and $\alpha = 1.0$. The refractive indices of red and pink lines are $1.50 + 0.001i$ and $1.50 + 0.005i$, respectively. For the comparison purpose, the data from the TAMUdust2020 was also included and the results calculated with (TAMU50) and without (TAMUfull) truncating the size distribution at $kx_m = 50$ are shown in (c).

wavelengths (e.g., 442 nm; Lin et al., 2018). Furthermore, this study found that these models could produce realistic $S - \delta$ joint distributions for lidar remote sensing applications at 355 nm.

As a sensitivity study, the relative errors in S and δ values due to truncating the size distribution at $kx_m = 50$ (hereafter, II-TM50 model) were investigated by using the II-TM results for $kx_m = 100$ (hereafter, II-TM100 model) in Figures 13a and 13b. Here we considered super-spheroid models with $n = 2.6$, 2.8, 3.0 and $\alpha = 0.5$, 1.0, 2.0 with refractive indices of $1.50 + i0.001$ and $1.50 + i0.005$. The super-spheroid models considered in this paper had maximum volume equivalent radius r_{max} ranging from 1.0 to 2.6 and 2.0 to 5.2 μm at $kx_m = 50$ and $kx_m = 100$, respectively (Figure 2a). These corresponded to a size parameter defined by $X_{\text{eq}} = 2\pi r_{\text{max}}/\lambda$ ranging from about 17.7–46.0 and 35.4–92.0 at $kx_m = 50$ and $kx_m = 100$, respectively. Among them, the models having the following r_{max} range were used for the sensitivity study, that is, $r_{\text{max}} = 1.0$–1.4 μm ($X_{\text{eq}} = 17.7$–24.8) and $r_{\text{max}} = 2.0$–2.8 μm ($X_{\text{eq}} = 35.4$–49.6) at $kx_m = 50$ and $kx_m = 100$, respectively. The largest r_{eff} ($r_{\text{eff,max}}$) values in each super-spheroid models ranged from 0.6 to 1.2 μm for the II-TM50 case.

In Figures 13a and 13b, the relative errors (R.E) in S and δ values of II-TM50 in respect to II-TM100 evaluated at the same r_{eff} are shown for each super-spheroid models. The horizontal axis shows the ratio of the r_{eff} value to the $r_{\text{eff,max}}$ value for each super-spheroid models in the form, $100r_{\text{eff}}/r_{\text{eff,max}}$. It was found that the S and δ values of II-TM50 were generally underestimated and overestimated, respectively (Figures 13a and 13b). The relative errors in S and δ increased as $r_{\text{eff}}/r_{\text{eff,max}}$ approached one on average, and the mean relative error of all models was about 10% for both S and δ at $r_{\text{eff}}/r_{\text{eff,max}} = 1$ (Figures 13a and 13b).

In order to investigate the overall trends in $S-\delta$ relation of large super-spheroid dust particles exceeding $kx_m = 100$, a combination of the II-TM ($kx_m = 0.1$–100) and IGOM ($kx_m = 100$–1,000) was used to compute the optical properties for the super-spheroid model with $n = 2.8$ and $\alpha = 1.0$ as a reference (hereafter, II-TM + IGOM), although the IGOM results are less accurate than the II-TM counterparts (Figure 13c). Note that the backscattering phase functions of IGOM were adjusted by following Ding et al. (2016) and Zhou and Yang (2015). The difference between the II-TM100 and II-TM + IGOM estimates in the r_{eff} range covered by II-TM50 is much smaller than those between II-TM100 and II-TM50 since large particles have less contribution to the results, for example, relative uncertainty in S, δ at $r_{\text{eff,max}}$ (II-TM50) ~1.0 μm for the super-spheroid model with $n = 2.8$, $\alpha = 1.0$ and $m = 1.50 + 0.001i$ are smaller than 3%. This also supports the use of II-TM100 as a reference solution for II-TM50 in Figures 13a and 13b.

The $S-\delta$ relation for II-TM50, II-TM100 and II-TM + IGOM was similar for small to moderate r_{eff} until the $S-\delta$ relation for II-TM + IGOM showed dramatic bending and increasing trends in S at large dust particle sizes (Figure 13c). Such turning point in the $S-\delta$ trend appeared at δ around 40% or larger, which corresponded to $r_{\text{eff}} > 2$ μm. The $S-\delta$ relation calculated from the TAMUdust2020 model ($0.1 \le kx_m \le 11,800$, $m = 1.50 + 0.003i$) for the case of degree of sphericity (Ψ) of 0.695 in Saito et al. (2021) is also shown in Figure 13c with and without truncating the size distribution at $kx_m = 50$. Although the shapes of TAMUdust2020 model are different, the general behaviors with respect to size was similar with the super-spheroids. The turning point of the $S-\delta$ trend for TAMUdust2020 model occurred at $\delta > 46\%$.

The $S-\delta$ values for the super-spheroid models with $m = 1.50 + 0.003i$ at large sizes are expected to be within the range between those for $m = 1.50 + 0.001i$ and $m = 1.50 + 0.005i$. The comparison of modeling results and observations (see Figures 9 and 10) could be improved if the backscattering optical properties of super-spheroids of large size parameters can be accurately obtained. Therefore, accurate computation of the backscattering properties of large super-spheroids is highly demanded and worthy of further studies.

4. Summary

We investigated the backscattering optical properties of dust at a wavelength of 355 nm, which has implications for the interpretation of future data from the ATLID instrument on the EarthCARE satellite. By employing the super-spheroid models, the optical properties of an ensemble of randomly oriented dust particles were calculated by the II-TM method. Intensive measurements of S and δ joint distributions from the NASA Langley HSRL-2 were used to investigate the applicability of the super-spheroid models for analysis of ATLID data.

We systematically examined the variations of the depolarization ratio (δ), lidar ratio (S), extinction coefficient (σ_{ext}), and backscattering coefficient (β) of the super-spheroid models with respect to two morphological parameters: aspect ratio (α) and roundness (n). In addition, the dependences of S and δ on the effective radius (r_{eff}) were examined. We found that σ_{ext} and β generally decreased as n increased mainly due to the decreasing cross section area. Additionally, the compact models with $\alpha = 1$ produced the largest σ_{ext} and β, whereas those with extreme α produced the smallest values. Differences in β among the models for the same r_{eff} exceeded one order of magnitude. S, which is the σ_{ext} to β ratio, increased with n. The models with α near 1 had the smallest S while those with extreme α had the largest. S decreased with increasing size at $r_{\text{eff}} > 0.1$ μm. In general, δ increased with r_{eff}. Particularly for models with small n (<2), δ reached its maximum at a small size (e.g., $r_{\text{eff}} = 0.4$ μm). Then, the r_{eff} dependence became weaker and δ declined slightly with size. For models with larger n (>2), δtended to increase linearly with size. Overall, models with $n > 2$ produced larger δ than those with $n < 2$, and the former showed smaller variability in δ due to α than the latter. $S-\delta$ relations were sensitive to the imaginary part of the refractive index (m_i). δ increased as m_i decreased, while S increased with m_i.

The super-spheroid models produced a wide range of $S-\delta$ relations. The majority of the S observed by HSRL varied between 40 and 60 Sr, values reported to be representative of Saharan regions. The measured δ values were mostly within the range for dust (20%–40%) reported in other studies. The super-spheroid models with different sets of n and α were capable of simulating the entire $S-\delta$ range of atmospheric dust obtained from the HSRL measurement at 355 nm. The $S-\delta$ relation could effectively discriminate dust from other particle types. The observed two-dimensional distribution of S and δ with moderate S (30–70 Sr) and δ (20%–40%) values, which had the largest population density, was best accounted for by models with $n > 2$, and especially by those with n varying from 2.4 to 3.0. The comparison of simulations with optimal shape parameters and the HSRL

observations indicated that the effective radius of dust particles in the 2014 measurements was in the range of 0.2–0.6 μm, while dust particles could be larger than 0.8 μm in the 2018 measurements. In addition, we compared the present model with the TAMUdust2020 model and found that the TAMUdust2020 results were similar to those of super-spheroid models with large roundness parameters (e.g., 2.8 and 3.0) when $\delta = 20\%$–40% (Figure 9). Furthermore, when the sensitivity of the $S - \delta$ relation to the imaginary part of the refractive index (m_i) and the truncation at $kx_m = 50$ was considered, the models with $n = 2.4$ to 3.0 and α near 1 were more optimal.

As $S - \delta$ relations at 355 nm will be used for aerosol classification and aerosol extinction retrievals for EarthCARE ATLID, this study suggests that super-spheroid models could be useful in dust microphysics retrieval and should be worthy of further applications. The super-spheroid models can be used not only for simulating dust, but also for simulating other particles including sea salts and ice crystals (Bi, Lin, Wang, et al., 2018; Sun et al., 2021). Thus, it may also be helpful to apply super-spheroid models to distinguish other aerosols and estimate their mixing ratios. The limitations of this study are that it did not consider inhomogeneity of composition and the size range of dust particles in the II-TM computation was relatively small. However, the components are essential for aerosol backscattering due to the wide variation of the refractive index (Zong et al., 2021), and inhomogeneous super-spheroid models are believed to exhibit a different S and δ, which could enhance the performances of super-spheroid models in simulating mineral dust aerosols. This work requires a higher computational cost to calculate the optical properties of more complex models, and the more accurate refractive indices of different mineral components are also demanding.

Data Availability Statement

The T-matrix data presented in this paper can be found at https://zenodo.org/record/5767741.

Acknowledgments
The authors acknowledge the NOAA Air Resources Laboratory (ARL) for the provision of the HYSPLIT transport and dispersion model and READY website (https://www.ready.noaa.gov), and the scattering properties obtained from TAMUdust2020. The authors also acknowledge the DISCOVER-AQ NASA LaRC HSRL2 data used in this study publicly available at https://www-air.larc.nasa.gov/cgi-bin/ArcView/discover-aq.co-2014?B200=1, and ORACLES Science Team (2020), Moffett Field, CA, NASA Ames Earth Science Project Office (ESPO) for the ORACLES P-3 Orion HSRL2 data used in this study publicly available at doi:10.5067/Suborbital/ORACLES/P3/2018_V2. K. Sato was supported by The Japan Aerospace Exploration Agency (EarthCARE satellite mission); JSPS (KAKENHI grant JP17H06139); Shiseido Female Researcher Science Grant; Ministry of Education, Culture, Sports, Science and Technology (MEXT; Initiative for Realizing Diversity in the Research Environment); Collaborative Research Program of the Research Institute for Applied Mechanics, Kyushu University (Fukuoka, Japan). L. Bei was supported by National Natural Science Foundation of China (42022038). A portion of the computations was performed on the National Supercomputer Center in Guangzhou (NSCC-GZ) and the cluster at State Key Lab of CAD&CG at Zhejiang University.

References

Andreae, M. O., & Rosenfeld, D. (2008). Aerosol–cloud–precipitation interactions. Part 1. The nature and sources of cloud-active aerosols. *Earth-Science Reviews*, *89*(1), 13–41. https://doi.org/10.1016/j.earscirev.2008.03.001

Ansmann, A., Mattis, I., Müller, D., Wandinger, U., Radlach, M., Althausen, D., & Damoah, R. (2005). Ice formation in Saharan dust over central Europe observed with temperature/humidity/aerosol Raman lidar. *Journal of Geophysical Research*, *110*(D18). https://doi.org/10.1029/2004jd005000

Aoki, T., Tanaka, T. Y., Uchiyama, A., Chiba, M., Mikami, M., Yabuki, S., & Key, J. R. (2005). Sensitivity experiments of direct radiative forcing caused by mineral dust simulated with a chemical transport model. *Journal of the Meteorological Society of Japan Series II*, *83A*, 315–331. https://doi.org/10.2151/jmsj.83A.315

Barr, A. H. (1981). Superquadrics and angle-preserving transformations. *IEEE Computer Graphics and Applications*, *1*(01), 11–23. https://doi.org/10.1109/MCG.1981.1673799

Bi, L., Ding, S., Zong, R., & Yi, B. (2020). Examining Asian dust refractive indices for brightness temperature simulations in the 650–1135 cm^{-1} spectral range. *Journal of Quantitative Spectroscopy and Radiative Transfer*, *247*, 106945. https://doi.org/10.1016/j.jqsrt.2020.106945

Bi, L., Lin, W., Liu, D., & Zhang, K. (2018). Assessing the depolarization capabilities of nonspherical particles in a super-ellipsoidal shape space. *Optics Express*, *26*(2), 1726–1742. https://doi.org/10.1364/OE.26.001726

Bi, L., Lin, W., Wang, Z., Tang, X., Zhang, X., & Yi, B. (2018). Optical modeling of sea salt aerosols: The effects of nonsphericity and inhomogeneity. *Journal of Geophysical Research: Atmospheres*, *123*(1), 543–558. https://doi.org/10.1002/2017jd027869

Bi, L., & Yang, P. (2014). Accurate simulation of the optical properties of atmospheric ice crystals with the invariant imbedding T-matrix method. *Journal of Quantitative Spectroscopy and Radiative Transfer*, *138*, 17–35. https://doi.org/10.1016/j.jqsrt.2014.01.013

Bi, L., & Yang, P. (2017). Improved ice particle optical property simulations in the ultraviolet to far-infrared regime. *Journal of Quantitative Spectroscopy and Radiative Transfer*, *189*, 228–237. https://doi.org/10.1016/j.jqsrt.2016.12.007

Bi, L., Yang, P., Kattawar, G. W., & Mishchenko, M. I. (2013). Efficient implementation of the invariant imbedding T-matrix method and the separation of variables method applied to large nonspherical inhomogeneous particles. *Journal of Quantitative Spectroscopy and Radiative Transfer*, *116*, 169–183. https://doi.org/10.1016/j.jqsrt.2012.11.014

Brunekreef, B., & Holgate, S. T. (2002). Air pollution and health. *The Lancet*, *360*(9341), 1233–1242. https://doi.org/10.1016/S0140-6736(02)11274-8

Burton, S. P., Ferrare, R. A., Hostetler, C. A., Hair, J. W., Rogers, R. R., Obland, M. D., et al. (2012). Aerosol classification using airborne High Spectral Resolution Lidar measurements—Methodology and examples. *Atmospheric Measurement Techniques*, *5*, 73–98. https://doi.org/10.5194/amt-5-73-2012

Burton, S. P., Hair, J. W., Kahnert, M., Ferrare, R. A., Hostetler, C. A., Cook, A. L., et al. (2015). Observations of the spectral dependence of linear particle depolarization ratio of aerosols using NASA Langley airborne High Spectral Resolution Lidar. *Atmospheric Chemistry and Physics*, *15*(23), 13453–13473. https://doi.org/10.5194/acp-15-13453-2015

Dentener, F. J., Carmichael, G. R., Zhang, Y., Lelieveld, J., & Crutzen, P. J. (1996). Role of mineral aerosol as a reactive surface in the global troposphere. *Journal of Geophysical Research*, *101*(D17), 22869–22889. https://doi.org/10.1029/96jd01818

Di Biagio, C., Boucher, H., Caquineau, S., Chevaillier, S., Cuesta, J., & Formenti, P. (2014). Variability of the infrared complex refractive index of African mineral dust: Experimental estimation and implications for radiative transfer and satellite remote sensing. *Atmospheric Chemistry and Physics*, *14*(20), 11093–11116. https://doi.org/10.5194/acp-14-11093-2014

Di Biagio, C., Formenti, P., Balkanski, Y., Caponi, L., Cazaunau, M., Pangui, E., et al. (2019). Complex refractive indices and single-scattering albedo of global dust aerosols in the shortwave spectrum and relationship to size and iron content. *Atmospheric Chemistry and Physics*, *19*(24), 15503–15531. https://doi.org/10.5194/acp-19-15503-2019

Ding, J., Yang, P., Holz, R. E., Platnick, S., Meyer, K. G., Vaughan, M. A., et al. (2016). Ice cloud backscatter study and comparison with CALIPSO and MODIS satellite data. *Optics Express*, *24*(1), 620–636. https://doi.org/10.1364/OE.24.000620

Dubovik, O., Holben, B., Eck, T. F., Smirnov, A., Kaufman, Y. J., King, M. D., et al. (2002). Variability of absorption and optical properties of key aerosol types observed in worldwide locations. *Journal of the Atmospheric Sciences*, *59*(3), 590–608. https://doi.org/10.1175/1520-0469(2002)059<0590:VOAAOP>2.0.CO;2

Dubovik, O., & King, M. D. (2000). A flexible inversion algorithm for retrieval of aerosol optical properties from Sun and sky radiance measurements. *Journal of Geophysical Research*, *105*(D16), 20673–20696. https://doi.org/10.1029/2000jd900282

Dubovik, O., Sinyuk, A., Lapyonok, T., Holben, B. N., Mishchenko, M., Yang, P., et al. (2006). Application of spheroid models to account for aerosol particle nonsphericity in remote sensing of desert dust. *Journal of Geophysical Research*, *111*(D11). https://doi.org/10.1029/2005jd006619

Duce, R. A., Liss, P. S., Merrill, J. T., Atlas, E. L., Buat-Menard, P., Hicks, B. B., et al. (1991). The atmospheric input of trace species to the world ocean. *Global Biogeochemical Cycles*, *5*(3), 193–259. https://doi.org/10.1029/91gb01778

Filioglou, M., Giannakaki, E., Backman, J., Kesti, J., Hirsikko, A., Engelmann, R., et al. (2020). Optical and geometrical aerosol particle properties over the United Arab Emirates. *Atmospheric Chemistry and Physics*, *20*(14), 8909–8922. https://doi.org/10.5194/acp-20-8909-2020

Freudenthaler, V., Esselborn, M., Wiegner, M., Heese, B., Tesche, M., Ansmann, A., et al. (2009). Depolarization ratio profiling at several wavelengths in pure Saharan dust during SAMUM 2006. *Tellus B: Chemical and Physical Meteorology*, *61*(1), 165–179. https://doi.org/10.1111/j.1600-0889.2008.00396.x

Gasteiger, J., Wiegner, M., Groß, S., Freudenthaler, V., Toledano, C., Tesche, M., & Kandler, K. (2011). Modelling lidar-relevant optical properties of complex mineral dust aerosols. *Tellus B: Chemical and Physical Meteorology*, *63*(4), 725–741. https://doi.org/10.1111/j.1600-0889.2011.00559.x

Ginoux, P., Chin, M., Tegen, I., Prospero, J. M., Holben, B., Dubovik, O., & Lin, S.-J. (2001). Sources and distributions of dust aerosols simulated with the GOCART model. *Journal of Geophysical Research*, *106*(D17), 20255–20273. https://doi.org/10.1029/2000jd000053

Groß, S., Freudenthaler, V., Schepanski, K., Toledano, C., Schäfler, A., Ansmann, A., & Weinzierl, B. (2015). Optical properties of long-range transported Saharan dust over Barbados as measured by dual-wavelength depolarization Raman lidar measurements. *Atmospheric Chemistry and Physics*, *15*(19), 11067–11080. https://doi.org/10.5194/acp-15-11067-2015

Groß, S., Tesche, M., Freudenthaler, V., Toledano, C., Wiegner, M., Ansmann, A., et al. (2011). Characterization of Saharan dust, marine aerosols and mixtures of biomass-burning aerosols and dust by means of multi-wavelength depolarization and Raman lidar measurements during SAMUM 2. *Tellus B: Chemical and Physical Meteorology*, *63*(4), 706–724. https://doi.org/10.1111/j.1600-0889.2011.00556.x

Haarig, M., Ansmann, A., Althausen, D., Klepel, A., Groß, S., Freudenthaler, V., et al. (2017). Triple-wavelength depolarization-ratio profiling of Saharan dust over Barbados during SALTRACE in 2013 and 2014. *Atmospheric Chemistry and Physics*, *17*(17), 10767–10794. https://doi.org/10.5194/acp-17-10767-2017

Hair, J. W., Hostetler, C. A., Cook, A. L., Harper, D. B., Ferrare, R. A., Mack, T. L., et al. (2008). Airborne high spectral resolution lidar for profiling aerosol optical properties. *Applied Optics*, *47*(36), 6734. https://doi.org/10.1364/AO.47.006734

Hansen, J. E. (1971). Multiple scattering of polarized light in planetary atmospheres Part II. Sunlight reflected by terrestrial water clouds. *Journal of the Atmospheric Sciences*, *28*(8), 1400–1426. https://doi.org/10.1175/1520-0469(1971)028<1400:MSOPLI>2.0.CO;2

Hansen, J. E., & Travis, L. D. (1974). Light scattering in planetary atmospheres. *Space Science Reviews*, *16*(4), 527–610. https://doi.org/10.1007/BF00168069

Haywood, J., Francis, P., Osborne, S., Glew, M., Loeb, N., Highwood, E., et al. (2003). Radiative properties and direct radiative effect of Saharan dust measured by the C-130 aircraft during SHADE: 1. Solar spectrum. *Journal of Geophysical Research*, *108*(D18). https://doi.org/10.1029/2002jd002687

Hess, M., Koepke, P., & Schult, I. (1998). Optical properties of aerosols and clouds: The software package OPAC. *Bulletin of the American Meteorological Society*, *79*(5), 14. https://doi.org/10.1175/1520-0477(1998)079<0831:OPOAAC>2.0.CO;2

Hofer, J., Althausen, D., Abdullaev, S. F., Makhmudov, A. N., Nazarov, B. I., Schettler, G., et al. (2017). Long-term profiling of mineral dust and pollution aerosol with multiwavelength polarization Raman lidar at the Central Asian site of Dushanbe, Tajikistan: Case studies. *Atmospheric Chemistry and Physics*, *17*(23), 14559–14577. https://doi.org/10.5194/acp-17-14559-2017

Hofer, J., Ansmann, A., Althausen, D., Engelmann, R., Baars, H., Fomba, K. W., et al. (2020). Optical properties of Central Asian aerosol relevant for spaceborne lidar applications and aerosol typing at 355 and 532 nm. *Atmospheric Chemistry and Physics*, *20*(15), 9265–9280. https://doi.org/10.5194/acp-20-9265-2020

Illingworth, A. J., Barker, H. W., Beljaars, A., Ceccaldi, M., Chepfer, H., Clerbaux, N., et al. (2015). The EarthCARE satellite: The next step forward in global measurements of clouds, aerosols, precipitation, and radiation. *Bulletin of the American Meteorological Society*, *96*(8), 1311–1332. https://doi.org/10.1175/BAMS-D-12-00227.1

Ishimoto, H., Zaizen, Y., Uchiyama, A., Masuda, K., & Mano, Y. (2010). Shape modeling of mineral dust particles for light- scattering calculations using the spatial poisson-voronoi tessellation. *Journal of Quantitative Spectroscopy and Radiative Transfer*, *111*, 2434–2443. https://doi.org/10.1016/j.jqsrt.2010.06.018

Järvinen, E., Kemppinen, O., Nousiainen, T., Kociok, T., Möhler, O., Leisner, T., & Schnaiter, M. (2016). Laboratory investigations of mineral dust near-backscattering depolarization ratios. *Journal of Quantitative Spectroscopy and Radiative Transfer*, *178*, 192–208. https://doi.org/10.1016/j.jqsrt.2016.02.003

Jin, Y., Nishizawa, T., Sugimoto, N., Ishii, S., Aoki, M., Sato, K., & Okamoto, H. (2020). Development of a 355-nm high-spectral-resolution lidar using a scanning Michelson interferometer for aerosol profile measurement. *Optics Express*, *28*(16), 23209–23222. https://doi.org/10.1364/OE.390987

Kaufman, Y. J., Tanre, D., Leon, J. -F., & Pelon, J. (2003). Retrievals of profiles of fine and coarse aerosols using lidar and radiometric space measurements. *IEEE Transactions on Geoscience and Remote Sensing*, *41*(8), 1743–1754. https://doi.org/10.1109/TGRS.2003.814138

Kim, M. -H., Kim, S. -W., & Omar, A. H. (2020). Dust lidar ratios retrieved from the CALIOP measurements using the MODIS AOD as a constraint. *Remote Sensing*, *12*(2), 251. https://doi.org/10.3390/rs12020251

Kim, M. -H., Omar, A. H., Tackett, J. L., Vaughan, M. A., Winker, D. M., Trepte, C. R., et al. (2018). The CALIPSO version 4 automated aerosol classification and lidar ratio selection algorithm. *Atmospheric Measurement Techniques*, *11*, 6107–6135. https://doi.org/10.5194/amt-11-6107-2018

Kok, J. F., Ridley, D. A., Zhou, Q., Miller, R. L., Zhao, C., Heald, C. L., et al. (2017). Smaller desert dust cooling effect estimated from analysis of dust size and abundance. *Nature Geoscience*, *10*(4), 274–278. https://doi.org/10.1038/ngeo2912

Levin, Z., Ganor, E., & Gladstein, V. (1996). The effects of desert particles coated with sulfate on rain formation in the Eastern Mediterranean. *Journal of Applied Meteorology and Climatology*, *35*(9), 1511–1523. https://doi.org/10.1175/1520-0450(1996)035<1511:TEODPC>2.0.CO;2

Lin, W., Bi, L., & Dubovik, O. (2018). Assessing superspheroids in modeling the scattering matrices of dust aerosols. *Journal of Geophysical Research: Atmospheres*, *123*(24), 13917–13943. https://doi.org/10.1029/2018jd029464

Lin, W., Bi, L., Weng, F., Li, Z., & Dubovik, O. (2021). Capability of superspheroids for modeling PARASOL observations under dusty-sky conditions. *Journal of Geophysical Research: Atmospheres*, *126*(1), e2020JD033310. https://doi.org/10.1029/2020jd033310

Linke, C., Möhler, O., Veres, A., Mohácsi, Á., Bozóki, Z., Szabó, G., & Schnaiter, M. (2006). Optical properties and mineralogical composition of different Saharan mineral dust samples: A laboratory study. *Atmospheric Chemistry and Physics*, *6*(11), 3315–3323. https://doi.org/10.5194/acp-6-3315-2006

Liu, Z., Sugimoto, N., & Murayama, T. (2002). Extinction-to-backscatter ratio of Asian dust observed with high-spectral-resolution lidar and Raman lidar. *Applied Optics*, *41*, 2760–2767. https://doi.org/10.1364/AO.41.002760

Mahowald, N., Albani, S., Kok, J. F., Engelstaeder, S., Scanza, R., Ward, D. S., & Flanner, M. G. (2014). The size distribution of desert dust aerosols and its impact on the Earth system. *Aeolian Research*, *15*, 53–71. https://doi.org/10.1016/j.aeolia.2013.09.002

Mahowald, N., Kohfeld, K., Hansson, M., Balkanski, Y., Harrison, S., Prentice, I., et al. (1999). Dust sources and deposition during the last glacial maximum and current climate: A comparison of model results with paleodata from ice cores and marine sediments. *Journal of Geophysical Research*, *104*, 15895–15916. https://doi.org/10.1029/1999JD900084

Mahowald, N. M., Baker, A. R., Bergametti, G., Brooks, N., Duce, R. A., Jickells, T. D., et al. (2005). Atmospheric global dust cycle and iron inputs to the ocean. *Global Biogeochemical Cycles*, *19*(4). https://doi.org/10.1029/2004gb002402

Mamouri, R.-E., & Ansmann, A. (2017). Potential of polarization/Raman lidar to separate fine dust, coarse dust, maritime, and anthropogenic aerosol profiles. *Atmospheric Measurement Techniques Discussions*, 1–41. https://doi.org/10.5194/amt-2017-131

Mamouri, R. E., Ansmann, A., Nisantzi, A., Kokkalis, P., Schwarz, A., & Hadjimitsis, D. (2013). Low Arabian dust extinction-to-backscatter ratio. *Geophysical Research Letters*, *40*(17), 4762–4766. https://doi.org/10.1002/grl.50898

Martin, J. H. (1990). Glacial-interglacial CO_2 change: The iron hypothesis. *Paleoceanography*, *5*(1), 1–13. https://doi.org/10.1029/pa005i001p00001

Mattis, I., Ansmann, A., Müller, D., Wandinger, U., & Althausen, D. (2002). Dual-wavelength Raman lidar observations of the extinction-to-backscatter ratio of Saharan dust. *Geophysical Research Letters*, *29*(9), 2020–124. https://doi.org/10.1029/2002gl014721

Miffre, A., Mehri, T., Francis, M., & Rairoux, P. (2016). UV–VIS depolarization from Arizona test dust particles at exact backscattering angle. *Journal of Quantitative Spectroscopy and Radiative Transfer*, *169*, 79–90. https://doi.org/10.1016/j.jqsrt.2015.09.016

Mishchenko, M. I., & Hovenier, J. W. (1995). Depolarization of light backscattered by randomly oriented nonspherical particles. *Optics Letters*, *20*(12), 1356–1358. https://doi.org/10.1364/OL.20.001356

Mishchenko, M. I., & Sassen, K. (1998). Depolarization of lidar returns by small ice crystals: An application to contrails. *Geophysical Research Letters*, *25*(3), 309–312. https://doi.org/10.1029/97gl03764

Mona, L., Liu, Z., Müller, D., Omar, A., Papayannis, A., Pappalardo, G., et al. (2012). Lidar measurements for desert dust characterization: An overview. *Advances in Meteorology*, e356265. https://doi.org/10.1155/2012/356265

Müller, D., Ansmann, A., Mattis, I., Tesche, M., Wandinger, U., Althausen, D., & Pisani, G. (2007). Aerosol-type-dependent lidar ratios observed with Raman lidar. *Journal of Geophysical Research*, *112*(D16). https://doi.org/10.1029/2006jd008292

Müller, D., Wandinger, U., & Ansmann, A. (1999). Microphysical particle parameters from extinction and backscatter lidar data by inversion with regularization: Theory. *Applied Optics*, *38*(12), 2346–2357. https://doi.org/10.1364/AO.38.002346

Müller, T., Schladitz, A., Kandler, K., & Wiedensohler, A. (2011). Spectral particle absorption coefficients, single scattering albedos and imaginary parts of refractive indices from ground based in situ measurements at Cape Verde Island during SAMUM-2. *Tellus B: Chemical and Physical Meteorology*, *63*(4), 573–588. https://doi.org/10.1111/j.1600-0889.2011.00572.x

Müller, T., Schladitz, A., Massling, A., Kaaden, N., Kandler, K., & Wiedensohler, A. (2009). Spectral absorption coefficients and imaginary parts of refractive indices of Saharan dust during SAMUM-1. *Tellus B: Chemical and Physical Meteorology*, *61*(1), 79–95. https://doi.org/10.1111/j.1600-0889.2008.00399.x

Muñoz, O., Moreno, F., Guirado, D., Dabrowska, D. D., Volten, H., & Hovenier, J. W. (2012). The Amsterdam–Granada light scattering database. *Journal of Quantitative Spectroscopy and Radiative Transfer*, *113*(7), 565–574. https://doi.org/10.1016/j.jqsrt.2012.01.014

Nisantzi, A., Mamouri, R. E., Ansmann, A., Schuster, G. L., & Hadjimitsis, D. G. (2015). Middle East versus Saharan dust extinction-to-backscatter ratios. *Atmospheric Chemistry and Physics*, *15*(12), 7071–7084. https://doi.org/10.5194/acp-15-7071-2015

Nishizawa, T., Okamoto, H., Sugimoto, N., Matsui, I., Shimizu, A., & Aoki, K. (2007). An algorithm that retrieves aerosol properties from dual-wavelength polarized lidar measurements. *Journal of Geophysical Research*, *112*(D6). https://doi.org/10.1029/2006jd007435

Nishizawa, T., Okamoto, H., Takemura, T., Sugimoto, N., Matsui, I., & Shimizu, A. (2008). Aerosol retrieval from two-wavelength backscatter and one-wavelength polarization lidar measurement taken during the MR01K02 cruise of the R/V Mirai and evaluation of a global aerosol transport model. *Journal of Geophysical Research*, *113*(D21), 21201. https://doi.org/10.1029/2007JD009640

Nishizawa, T., Sugimoto, N., Matsui, I., Shimizu, A., & Okamoto, H. (2011). Algorithms to retrieve optical properties of three component aerosols from two-wavelength backscatter and one-wavelength polarization lidar measurements considering nonsphericity of dust. *Journal of Quantitative Spectroscopy and Radiative Transfer*, *112*(2), 254–267. https://doi.org/10.1016/j.jqsrt.2010.06.002

Nishizawa, T., Sugimoto, N., Matsui, I., Shimizu, A., Tatarov, B., & Okamoto, H. (2008). Algorithm to retrieve aerosol optical properties from high-spectral-resolution lidar and polarization Mie-scattering lidar measurements. *IEEE Transactions on Geoscience and Remote Sensing*, *46*(12), 4094–4103. https://doi.org/10.1109/tgrs.2008.2000797

Noh, Y. M., Kim, Y. J., & Müller, D. (2008). Seasonal characteristics of lidar ratios measured with a Raman lidar at Gwangju, Korea in spring and autumn. *Atmospheric Environment*, *42*(9), 2208–2224. https://doi.org/10.1016/j.atmosenv.2007.11.045

Okamoto, H., Sato, K., Borovoi, A., Ishimoto, H., Masuda, K., Konoshonkin, A., & Kustova, N. (2019). Interpretation of lidar ratio and depolarization ratio of ice clouds using spaceborne high-spectral-resolution polarization lidar. *Optics Express*, *27*(25), 36587–36600. https://doi.org/10.1364/OE.27.036587

Okamoto, H., Sato, K., Borovoi, A., Ishimoto, H., Masuda, K., Konoshonkin, A., & Kustova, N. (2020). Wavelength dependence of ice cloud backscatter properties for space-borne polarization lidar applications. *Optics Express*, *28*(20), 29178–29191. https://doi.org/10.1364/OE.400510

Omar, A. H., Winker, D. M., Vaughan, M. A., Hu, Y., Trepte, C. R., Ferrare, R. A., et al. (2009). The CALIPSO automated aerosol classification and lidar ratio selection algorithm. *Journal of Atmospheric and Oceanic Technology*, *26*(10), 1994–2014. https://doi.org/10.1175/2009JTECHA1231.1

Papayannis, A., Balis, D., Amiridis, V., Chourdakis, G., Tsaknakis, G., Zerefos, C., et al. (2005). Measurements of Saharan dust aerosols over the Eastern Mediterranean using elastic backscatter-Raman lidar, spectrophotometric and satellite observations in the frame of the EARLINET project. *Atmospheric Chemistry and Physics*, *5*, 2065–2079. https://doi.org/10.5194/acp-5-2065-2005

Patterson, E. M., Gillette, D. A., & Stockton, B. H. (1977). Complex index of refraction between 300 and 700 nm for Saharan aerosols 1896–1977. *Journal of Geophysical Research*, *82*(21), 3153–3160. https://doi.org/10.1029/jc082i021p03153

Péré, J.-C., Rivellini, L., Crumeyrolle, S., Chiapello, I., Minvielle, F., Thieuleux, F., et al. (2018). Simulation of African dust properties and radiative effects during the 2015 SHADOW campaign in Senegal. *Atmospheric Research*, *199*, 14–28. https://doi.org/10.1016/j.atmosres.2017.07.027

Preißler, J., Wagner, F., Pereira, S. N., & Guerrero-Rascado, J. L. (2011). Multi-instrumental observation of an exceptionally strong Saharan dust outbreak over Portugal. *Journal of Geophysical Research*, *116*(D24). https://doi.org/10.1029/2011jd016527

Prospero, J., Ginoux, P., Torres, O., Nicholson, S., & Gill, T. (2002). Environmental characterization of global sources of atmospheric soil dust identified with the NIMBUS 7 Total Ozone Mapping Sectrometer (TOMS) absorbing aerosol product. *Reviews of Geophysics*, *40*, 2–1. https://doi.org/10.1029/2000RG000095

Redemann, J., Wood, R., Zuidema, P., Doherty, S. J., Luna, B., LeBlanc, S. E., et al. (2021). An overview of the ORACLES (ObseRvations of Aerosols above CLouds and their intEractionS) project: Aerosol–cloud–radiation interactions in the southeast Atlantic basin. *Atmospheric Chemistry and Physics*, *21*(3), 1507–1563. https://doi.org/10.5194/acp-21-1507-2021

Reid, E. A., Reid, J. S., Meier, M. M., Dunlap, M. R., Cliff, S. S., Broumas, A., et al. (2003). Characterization of African dust transported to Puerto Rico by individual particle and size segregated bulk analysis. *Journal of Geophysical Research*, *108*(D19). https://doi.org/10.1029/2002jd002935

Reid, J. S., Jonsson, H. H., Maring, H. B., Smirnov, A., Savoie, D. L., Cliff, S. S., et al. (2003). Comparison of size and morphological measurements of coarse mode dust particles from Africa. *Journal of Geophysical Research*, *108*(D19). https://doi.org/10.1029/2002jd002485

Rocha-Lima, A., Martins, J. V., Remer, L. A., Todd, M., Marsham, J. H., Engelstaedter, S., et al. (2018). A detailed characterization of the Saharan dust collected during the Fennec campaign in 2011: In situ ground-based and laboratory measurements. *Atmospheric Chemistry and Physics*, *18*(2), 1023–1043. https://doi.org/10.5194/acp-18-1023-2018

Rolph, G., Stein, A., & Stunder, B. (2017). Real-time Environmental Applications and Display sYstem: READY. *Environmental Modelling & Software*, *95*, 210–228. https://doi.org/10.1016/j.envsoft.2017.06.025

Saito, M., & Yang, P. (2021). Advanced bulk optical models linking the backscattering and microphysical properties of mineral dust aerosol. *Geophysical Research Letters*, *48*(17), e2021GL095121. https://doi.org/10.1029/2021GL095121

Saito, M., Yang, P., Ding, J., & Liu, X. (2021). A comprehensive database of the optical properties of irregular aerosol particles for radiative transfer simulations. *Journal of the Atmospheric Sciences*, *78*(7), 2089–2111. https://doi.org/10.1175/JAS-D-20-0338.1

Sakai, T., Nagai, T., Zaizen, Y., & Mano, Y. (2010). Backscattering linear depolarization ratio measurements of mineral, sea-salt, and ammonium sulfate particles simulated in a laboratory chamber. *Applied Optics*, *49*(23), 4441–4449. https://doi.org/10.1364/AO.49.004441

Sato, K., & Okamoto, H. (2011). Refinement of global ice microphysics using spaceborne active sensors. *Journal of Geophysical Research*, *116*(D20). https://doi.org/10.1029/2011JD015885

Sato, K., Okamoto, H., & Ishimoto, H. (2018). Physical model for multiple scattered space-borne lidar returns from clouds. *Optics Express*, *26*, A301–A319. https://doi.org/10.1364/OE.26.00A301

Sato, K., Okamoto, H., & Ishimoto, H. (2019). Modeling the depolarization of space-borne lidar signals. *Optics Express*, *27*, A117–A132. https://doi.org/10.1364/OE.27.00A117

Sato, K., Okamoto, H., Yamamoto, M. K., Fukao, S., Kumagai, H., Ohno, Y., et al. (2009). 95-GHz Doppler radar and lidar synergy for simultaneous ice microphysics and in-cloud vertical air motion retrieval. *Journal of Geophysical Research*, *114*(D3). https://doi.org/10.1029/2008JD010222

Schulz, M., Balkanski, Y. J., Guelle, W., & Dulac, F. (1998). Role of aerosol size distribution and source location in a three-dimensional simulation of a Saharan dust episode tested against satellite-derived optical thickness. *Journal of Geophysical Research*, *103*(D9), 10579–10592. https://doi.org/10.1029/97jd02779

Shettle, E., & Fenn, R. (1979). Models for the aerosols of the lower atmosphere and the effects of humidity variations on their optical properties. *Environmental Research*, *94*.

Shi, Z., Shao, L., Jones, T. P., & Lu, S. (2005). Microscopy and mineralogy of airborne particles collected during severe dust storm episodes in Beijing, China. *Journal of Geophysical Research*, *110*(D1). https://doi.org/10.1029/2004jd005073

Shin, S.-K., Tesche, M., Kim, K., Kezoudi, M., Tatarov, B., Müller, D., & Noh, Y. (2018). On the spectral depolarisation and lidar ratio of mineral dust provided in the AERONET version 3 inversion product. *Atmospheric Chemistry and Physics*, *18*(17), 12735–12746. https://doi.org/10.5194/acp-18-12735-2018

Sokolik, I. N., & Toon, O. B. (1999). Incorporation of mineralogical composition into models of the radiative properties of mineral aerosol from UV to IR wavelengths. *Journal of Geophysical Research*, *104*(D8), 9423–9444. https://doi.org/10.1029/1998jd200048

Sroga, J. T., Eloranta, E. W., Shipley, S. T., Roesler, F. L., & Tryon, P. J. (1983). High spectral resolution lidar to measure optical scattering properties of atmospheric aerosols. 2: Calibration and data analysis. *Applied Optics*, *22*(23), 3725–3732. https://doi.org/10.1364/AO.22.003725

Stegmann, P. G., & Yang, P. (2017). A regional, size-dependent, and causal effective medium model for Asian and Saharan mineral dust refractive index spectra. *Journal of Aerosol Science*, *114*, 327–341. https://doi.org/10.1016/j.jaerosci.2017.10.003

Stein, A. F., Draxler, R. R., Rolph, G. D., Stunder, B. J. B., Cohen, M. D., & Ngan, F. (2015). NOAA's HYSPLIT atmospheric transport and dispersion modeling system. *Bulletin of the American Meteorological Society*, *96*, 2059–2077. https://doi.org/10.1175/bams-d-14-00110.1

Sugimoto, N., & Lee, C. H. (2006). Characteristics of dust aerosols inferred from lidar depolarization measurements at two wavelengths. *Applied Optics*, *45*(28), 7468. https://doi.org/10.1364/AO.45.007468

Sun, L., Bi, L., & Yi, B. (2021). The use of superspheroids as surrogates for modeling electromagnetic wave scattering by ice crystals. *Remote Sensing*, *13*(9), 1733. https://doi.org/10.3390/rs13091733

Tang, X., Bi, L., Lin, W., Liu, D., Zhang, K., & Li, W. (2019). Backscattering ratios of soot-contaminated dusts at triple LiDAR wavelengths: T-Matrix results. *Optics Express*, *27*(4), A92–A116. https://doi.org/10.1364/OE.27.000A92

Tegen, I., Hollrig, P., Chin, M., Fung, I., Jacob, D., & Penner, J. (1997). Contribution of different aerosol species to the global aerosol extinction optical thickness: Estimates from model results. *Journal of Geophysical Research*, *102*(D20), 23895–23915. https://doi.org/10.1029/97jd01864

Tesche, M., Ansmann, A., Müller, D., Althausen, D., Mattis, I., Heese, B., et al. (2009). Vertical profiling of Saharan dust with Raman lidars and airborne HSRL in southern Morocco during SAMUM. *Tellus B: Chemical and Physical Meteorology*, *61*(1), 144–164. https://doi.org/10.1111/j.1600-0889.2008.00390.x

Veselovskii, I., Dubovik, O., Kolgotin, A., Korenskiy, M., Whiteman, D. N., Allakhverdiev, K., & Huseyinoglu, F. (2012). Linear estimation of particle bulk parameters from multi-wavelength lidar measurements. *Atmospheric Measurement Techniques*, *5*(5), 1135–1145. https://doi.org/10.5194/amt-5-1135-2012

Veselovskii, I., Dubovik, O., Kolgotin, A., Lapyonok, T., Girolamo, P. D., Summa, D., et al. (2010). Application of randomly oriented spheroids for retrieval of dust particle parameters from multiwavelength lidar measurements. *Journal of Geophysical Research*, *115*(D21). https://doi.org/10.1029/2010jd014139

Veselovskii, I., Goloub, P., Podvin, T., Bovchaliuk, V., Derimian, Y., Augustin, P., et al. (2016). Retrieval of optical and physical properties of African dust from multiwavelength Raman lidar measurements during the SHADOW campaign in Senegal. *Atmospheric Chemistry and Physics*, *16*(11), 7013–7028. https://doi.org/10.5194/acp-16-7013-2016

Veselovskii, I., Hu, Q., Goloub, P., Podvin, T., Korenskiy, M., Derimian, Y., et al. (2020). Variability in lidar-derived particle properties over West Africa due to changes in absorption: Towards an understanding. *Atmospheric Chemistry and Physics*, *20*(11), 6563–6581. https://doi.org/10.5194/acp-20-6563-2020

Wagner, R., Ajtai, T., Kandler, K., Lieke, K., Linke, C., Müller, T., et al. (2012). Complex refractive indices of Saharan dust samples at visible and near UV wavelengths: A laboratory study. *Atmospheric Chemistry and Physics*, *12*(5), 2491–2512. https://doi.org/10.5194/acp-12-2491-2012

Wiegner, M., Groß, S., Freudenthaler, V., Schnell, F., & Gasteiger, J. (2011). The May/June 2008 Saharan dust event over Munich: Intensive aerosol parameters from lidar measurements. *Journal of Geophysical Research*, *116*(D23). https://doi.org/10.1029/2011jd016619

Winker, D. M., Pelon, J., Coakley, J. A., Ackerman, S. A., Charlson, R. J., Colarco, P. R., et al. (2010). The CALIPSO mission: A global 3D view of aerosols and clouds. *Bulletin of the American Meteorological Society*, *91*(9), 1211–1230. https://doi.org/10.1175/2010BAMS3009.1

Yang, P., & Liou, K. N. (1996). Geometric-optics–integral-equation method for light scattering by nonspherical ice crystals. *Applied Optics*, *35*(33), 6568–6584. https://doi.org/10.1364/AO.35.006568

Zender, C. S., Bian, H., & Newman, D. (2003). Mineral Dust Entrainment and Deposition (DEAD) model: Description and 1990s dust climatology. *Journal of Geophysical Research*, *108*(D14). https://doi.org/10.1029/2002jd002775

Zhou, C., & Yang, P. (2015). Backscattering peak of ice cloud particles. *Optics Express*, *23*(9), 11995–12003. https://doi.org/10.1364/OE.23.011995

Zong, R., Weng, F., Bi, L., Lin, X., Rao, C., & Li, W. (2021). Impact of hematite on dust absorption at wavelengths ranging from 0.2 to 1.0 μm: An evaluation of literature data using the T-matrix method. *Optics Express*, *29*(11), 17405–17427. https://doi.org/10.1364/OE.427611